

Sublimation of Laboratory Ices Millimeter/Submillimeter Experiment (SubLIME): Structure-Specific Identifications of Products from UV Photolyzed Methanol Ice

2 K. M. YOCUM ^{1,2,3} S. N. MILAM ³ P. A. GERAKINES ³ AND S. L. WIDICUS WEAVER ^{1,2}

3 ¹*Department of Chemistry, Emory University*
4 *1515 Dickey Dr. Atlanta, GA, 30322*

5 ²*Department of Chemistry, University of Wisconsin - Madison*
6 *1101 University Ave, Madison, WI 53706*

7 ³*Astrochemistry Laboratory, NASA Goddard Space Flight Center*
8 *8800 Greenbelt Rd, Greenbelt, MD 20771*

9 (Received December 17, 2020; Revised February XX, 2021; Accepted February 21, 2021)

10 Submitted to ApJ

11 ABSTRACT

12 Submillimeter/far-IR spectroscopy was used to detect and quantify organic molecules sublimated
13 after the ultraviolet photolysis (at 12 K) and warm-up (up to 300 K) of a methanol (CH₃OH) ice
14 sample. Eleven sublimed photoproducts were uniquely identified: carbon monoxide (CO), formalde-
15 hyde (H₂CO), ketene (C₂H₂O), acetaldehyde (CH₃CHO), ethylene oxide (CH₂OCH₂), vinyl alcohol
16 (CH₂CHOH), ethanol (CH₃CH₂OH), dimethyl ether (CH₃OCH₃), methyl formate (HCOOCH₃), gly-
17 colaldehyde (HOCH₂CHO), and acetone ((CH₃)₂CO). Two additional products were detected in the
18 photolyzed ice by FTIR spectroscopy: carbon dioxide (CO₂) and methane (CH₄). The rotational
19 temperatures and gas densities were calculated for the organics containing two or more C-atoms via
20 rotational diagram analysis, and the gas-phase submillimeter/far-IR technique was used in tandem
21 with mass spectrometry and FTIR spectroscopy of the ice during photolysis. The abundance ra-
22 tios of the sublimed species (normalized to methanol) were compared to those observed in hot cores
23 (Orion-KL, Sagittarius B2(N), and IRAS 16293-2422(B)) and in comets C/2014 Q2 (Lovejoy) and
24 67P/Churyumov–Gerasimenko.

25 *Keywords:* astrochemistry — molecular spectroscopy — experimental techniques — molecule formation
26

27 1. INTRODUCTION

28 In cold dense cores, icy dust grains are constantly bombarded with different forms of radiation that alter the
29 molecules in the ice by ionizing them and/or breaking them down into radicals. Those species recombine in different
30 configurations that in many cases result in more complex molecules than the original reactants. Those products
31 can then be ejected into the gas phase by different physical processes, including, but not limited to, heating from
32 nearby protostar formation, photodesorption caused by exposure to ultraviolet (UV) photons, reactive desorption, and
33 sputtering from cosmic ray collisions. In this way, there exists a close connection between ice chemistry and the gas
34 compositions of interstellar clouds, a relationship that remains only poorly understood. Furthermore, several volatile
35 organics that have been detected in the interstellar medium (ISM) have also been detected in comets, in some cases
36 with similar abundance ratios (Rubin et al. 2019a; Drozdovskaya et al. 2018; Bockelée-Morvan et al. 2000), providing
37 evidence for the preservation of organic species from the earliest stages of star formation to their incorporation in
38 comets and other icy solar system bodies such as Kuiper Belt Objects (KBOs).

Laboratory studies have demonstrated the importance of ice surface chemistry for complex organic formation in the ISM by providing necessary information (e.g., reaction rate constants, surface binding energies, formation mechanisms, branching ratios) to improve the accuracy of computational models (Paulive et al. 2020; Bergantini et al. 2018; Shingledecker & Herbst 2018; Abplanalp et al. 2016). Methanol (CH_3OH), plays an important role in this chemistry, because once dissociated it provides functional groups CH_3 , OH , CH_3O , and CH_2OH that can be used to build larger organics, and it is abundant in both interstellar and cometary ices. Laboratory studies of the energetic processing (e.g., UV photolysis, electron and proton irradiation) of ices containing methanol have predicted formation pathways for larger organics such as ethanol ($\text{CH}_3\text{CH}_2\text{OH}$) (Abou Mrad et al. 2016; Henderson & Gudipati 2015; Öberg et al. 2009), dimethyl ether (CH_3OCH_3) (Abou Mrad et al. 2016; Öberg et al. 2009), methyl formate (HCOOCH_3) (Abou Mrad et al. 2016; Henderson & Gudipati 2015; Öberg et al. 2009; Gerakines et al. 1996), glycolaldehyde (HOCH_2CHO) (Henderson & Gudipati 2015; Öberg et al. 2009), acetic acid (CH_3COOH) (Abou Mrad et al. 2016; Öberg et al. 2009), and many more upon sample warm-up. Many of these products are structural isomers built from the key functional groups of methanol.

The most common technique for gas-phase detections following ice sublimation is mass spectrometry, but the similarities in chemical structures between these products results in crowded mass spectra riddled with overlapping features. Coupling with gas chromatography provides a potential resolution of this issue, but the components of the sample must be known in order to determine the appropriate separation conditions for analysis (Abou Mrad et al. 2014). Therefore, laboratory studies require structure-specific techniques to distinguish and quantify structural isomers (e.g., $\text{C}_2\text{H}_6\text{O}$ and $\text{C}_2\text{H}_4\text{O}_2$) and to potentially uncover the carriers of as-yet-unassigned features of complex organic species in astronomical observations.

Rotational spectroscopy is a highly useful technique for measuring the compositions of complex gas mixtures. Gas-phase spectroscopy has been demonstrated as an in-situ detection method for desorbed laboratory ices at submillimeter/far-IR wavelengths (Yocum et al. 2019) and at microwave wavelengths (Theulé et al. 2020). Not only is this a non-invasive technique (i.e., the experimental and/or sample conditions are unaltered), but radio and far-IR spectroscopies are the most widely-used remote sensing techniques for probing the gas-phase compositions of interstellar clouds, cometary comae, and planetary atmospheres. The work presented here expands upon the submillimeter spectroscopic technique put forth by Yocum et al. (2019) by demonstrating the detection capabilities for sublimated UV photoproducts of methanol ice including the unique detections of the structural isomers $\text{C}_2\text{H}_4\text{O}$, $\text{C}_2\text{H}_6\text{O}$, and $\text{C}_2\text{H}_4\text{O}_2$. Secondly, the temperatures and densities of the detected photoproducts were determined via a rotation diagram analysis and compared to astronomical observations of complex organics detected in interstellar and cometary sources.

2. EXPERIMENTAL TECHNIQUES

All reported experiments were conducted using the laboratory setup described by Yocum et al. (2019).¹ The experimental setup consists of an ultra-high vacuum (UHV) chamber with a base pressure of $\sim 1 \times 10^{-9}$ Torr. Three changes to the previous design were implemented in the present study. First, the static UV lamp described in the previous study was replaced with a microwave-discharged hydrogen-flow lamp (MDHL) which is described in detail in Section 2.2. Secondly, a Fourier-transform infrared (FTIR) spectrometer was added to the system. Section 2.3 contains the details of the FTIR setup. Lastly, crystal quartz viewports (Kurt J. Lesker Co., VPZL-275UCQ) were used in place of the original sapphire viewports of the millimeter/submillimeter/far-IR spectrometer in order to increase the transmittance of the submillimeter/far-IR radiation through the windows into and out of the UHV chamber. All other aspects of the setup and the details of the equipment were as described by Yocum et al. (2019).

For the experiments performed here, ice samples were created at 12 K on a gold substrate attached to a closed-cycle helium cryostat and then were exposed to UV photons from the MDHL located on the port at the top of the chamber. After UV photolysis, the valves to the pumps were closed and the ices were heated slowly to 300 K in order to fully sublime the sample. The desorbed species were then detected with submillimeter/far-IR spectroscopy to identify UV photoproducts. Furthermore, a rotation diagram analysis was performed for each individual photoproduct to determine the rotational temperatures and gas densities relative to the amount of methanol detected. Each of these steps are presented in detail in the following sections.

¹ <https://science.gsfc.nasa.gov/691/sublime/index.html>

2.1. Ice Sample Creation

The methanol ice samples were formed by vapor deposition onto the cold substrate through a high-precision gas-dosing valve, maintaining a chamber pressure of 1.0×10^{-7} Torr for 20 min. The vapor was evaporated from 99.9% HPLC grade liquid methanol (Fisher Scientific, A452-4) that was degassed by three freeze-pump-thaw cycles. After the ice was formed, the chamber was pumped out until the pressure returned to the base pressure at the start of the experiment.

2.2. UV Photolysis and Thermal Processing of Ice Samples

The ice samples were exposed to the output of a microwave-discharged hydrogen-flow lamp (MDHL) that simulates the UV radiation field present in an interstellar cloud. The photons enter the chamber through a MgF₂ ConFlatTM viewport with an incidence angle of 13° at the surface of the ice. The MDHL has an F-type configuration and is constructed of quartz. Hydrogen gas was flowed through the lamp at pressures of ~ 450 mTorr and an Evenson cavity was used to spark a microwave discharge across the quartz lamp body. For all experiments, the microwave generator (Ophos MPG-4 526) forward power was 100 Watts and reflected power was ~ 0 -2 Watts. For a detailed description of MDHLs including the typical UV emission spectra for these UV lamps refer to [Chen et al. \(2013\)](#). The average flux of the UV lamp was $6.0 \pm 1.0 \times 10^{13}$ photons cm⁻² s⁻¹, as was measured throughout the duration of one experiment via the technique described by [Fulvio et al. \(2014\)](#), utilizing the photoelectric effect of a gold wire suspended in the chamber about one inch above the ice sample. The methanol ice sample was photolyzed for one hour, exposing the sample to a total fluence of $2.2 \pm 0.35 \times 10^{17}$ photons cm⁻².

After the methanol ice samples were photolyzed, the UV lamp was turned off, the valve to the pump was closed, and the ice was slowly heated from 12 to 300 K at 1 K min⁻¹. The cryostat was turned off during the ice warm-up to minimize recondensation. Infrared spectra of the ice were collected simultaneously with mass spectra of the species that desorbed during the ice warm-up. These spectra were obtained in 10 K increments.

2.3. Infrared Spectra of Methanol Ices

The methanol ice samples were monitored using IR spectroscopy during the UV photolysis and the warm-up procedure. IR spectra were collected with a Thermo Scientific NicoletTM iS50 FTIR spectrometer via the reflection-absorption infrared spectroscopy (RAIRS) technique. The IR beam enters the chamber through a ZeSe viewport (Kurt J. Lesker) with a $\sim 77^\circ$ angle of incidence where it is reflected from the gold surface, exits the chamber through a second ZeSe viewport, and is detected by a liquid-nitrogen cooled mercury-cadmium-telluride (MCT) detector.

IR spectra were collected in 10-min intervals during photolysis from the MDHL. After being photolyzed, the ices were slowly heated to 300 K and IR spectra were collected every 10 K to determine the temperatures at which specific IR features changed and to ensure full sublimation of the ice sample.

2.4. Submillimeter/far-IR Spectra of Sublimated UV-Photolyzed Methanol Ices

A thorough description of the millimeter/submillimeter/far-IR spectrometer has been given by [Yocum et al. \(2019\)](#) and the references therein. In brief, the spectral range covers 70-1000 GHz, 1.8-1.9 THz, and 2.5-2.6 THz. The setup uses lock-in amplification to improve signal-to-noise ratio. The input radiation was frequency-modulated at 0.2 kHz with a modulation depth of 75 kHz. This is a phase-sensitive detection technique which results in 2f spectral line shapes. All spectra were collected with 0.1-MHz resolution, and the number of spectral averages varied based on the experimental approach (broadband vs. targeted searches) and the detection limits of the molecules of interest.

Gas-phase direct-absorption submillimeter/far-IR spectra were collected for the species desorbed from the photolyzed methanol ices. By closing the gate valve between the chamber and the turbomolecular pump, the desorbed species were trapped in the main vacuum chamber while spectra were measured. While the system remained at ~ 300 K, broadband spectra were collected between 758-926 GHz and any absorption peak with a signal-to-noise ratio ≥ 5 was considered a detection.

After identification of several photoproducts from the broadband submillimeter spectra, more sensitive, targeted searches were carried out to search for weaker species that may have been present. The targeted searches spanned ~ 10 MHz-wide spectral windows with the specific transition frequency of a given species set at the center of the spectral window. The number of spectral averages varied for each targeted search, based on the spectral power at a given frequency, the intensity of the peaks of the specific species, and its relative abundance. Some detections only required 30 averages while others required up to 200 averages. The selected transitions were determined based on a list

of criteria: spectral power, reported intensity of the target transition, and lack of overlap with methanol or potential photoproducts. It is important to note that the spectrometer does not generate power across the entire 70-1000 GHz range. There are several small regions where there was little to no signal produced by the light source. The output spectral power was therefore the first criterion for potential detection, and only regions with sufficient power in this system were selected. Secondly, the detection limits of this technique in terms of peak intensity were determined throughout the project for each specific photoproduct. Lastly, complex mixtures have submillimeter spectra that can be crowded, causing blending between different transitions of varying photoproducts. With all three of these criteria in mind, the selected transitions correspond to the combination of highest spectral power + largest peak intensity + resolved transitions.

2.5. Standards and Background Tests

Molecular standards were used for spectral assignments in the solid-phase RAIRS spectra and in the gas-phase submillimeter/far-IR spectra. The IR spectra were assigned by comparison to reference FTIR spectra of acetaldehyde (Hudson & Ferrante 2019), acetone (Hudson et al. 2018), acetic acid, dimethyl ether (Hudson et al. 2020), ethanol (Hudson 2017), ethylene glycol (Hudson et al. 2005), formaldehyde (Gerakines et al. 1996), formic acid, glycolaldehyde (Hudson et al. 2005), and methyl formate (Modica & Palumbo 2010). The majority of the spectral assignments for the gas-phase spectra were aided by simulated spectra from online spectral databases including the JPL² and CDMS³ catalogs. Molecular searches were also conducted through comparison with Splatalogue⁴, which combines spectral catalog information from multiple spectral databases.

Gas-phase reference spectra were collected of acetaldehyde due to several missing transitions in the online databases and the large uncertainties of the transition frequencies that are reported. These reference spectra were collected by adding a small amount of acetaldehyde vapor into the chamber. The chamber was filled to ~ 1.0 mTorr, and spectra were collected over all spectral windows to confirm that peaks assigned to other photoproducts were not those of acetaldehyde. Reference spectra were also collected for methanol, even though the spectral catalogs for methanol and its isotopologues are thoroughly studied. This was done to verify that no higher vibrational states of methanol and its isotopologues were present, considering the spectral catalogs were calculated for $v = 2$ and lower. Therefore, all detections reported were checked against methanol and acetaldehyde reference spectra.

Two submillimeter background tests were conducted to ensure that all of the detected transitions originated from species desorbed from the photolyzed methanol ice and not from residual gases in the UHV chamber. The first test involved experiments that replicated the UV photolysis and warm-up procedure with no ice present to ensure all detected photoproducts came from the photolyzed ice. From this test, the only background contamination detected by the millimeter/submillimeter/far-IR spectrometer after warm-up was a small amount of carbon monoxide, CO. No CO was detected by the FTIR spectrometer at a substrate temperature of 12 K. The origin of background CO was likely due to outgassing of the chamber walls and other chamber components when the gate valve was closed to the pumps. The second background test was conducted to confirm that no photoproduct transitions were detected without exposure to UV radiation. These experiments replicated the ice deposition and warm-up procedures without running the UV lamp. The only background contamination, again, was a small amount of CO. This background CO was quantified and subtracted from the experimental data presented here. Mass spectrometer background scans at the beginning of daily experiments showed trace amounts of H₂, H₂O, CO, and CO₂ (less than $\sim 3.2 \times 10^7$ molec. cm⁻³).

3. RESULTS AND ANALYSIS

Several photoproducts were produced in the 12 K ice after the one-hour UV-photolysis and were detected with the FTIR spectrometer. The submillimeter spectroscopic detection of additional photoproducts occurred after the ice warm-up to 300 K under static vacuum. In this section, the photoproducts detected in the ice at 12 K are presented in Section 3.1, changes in the IR spectra during ice warm-up from 12 to 300 K are presented in Section 3.2, all photoproducts detected after warm-up to 300 K are presented in Section 3.3, and their respective rotational-diagram analyses can be found in Section 3.4.

² spec.jpl.nasa.gov

³ cdms.astro.uni-koeln.de/classic

⁴ splatalogue.online

3.1. Low Temperature UV Photolysis at 12 K

Chemical changes of the methanol ice were captured in IR spectra every 10 min as the ice was photolyzed for one hour. Figure 1 shows IR spectra of the background before ice deposition (No ice), methanol ice before (0 min), during (10-50 min), and after (60 min) the one-hour UV exposure.

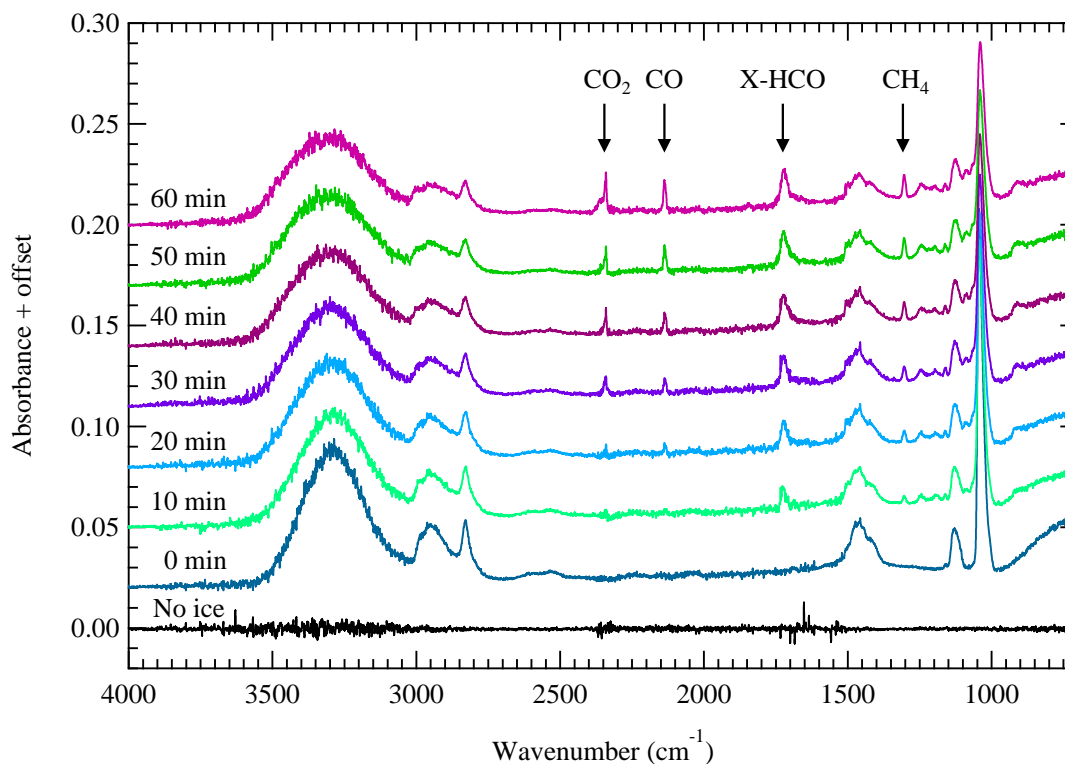


Figure 1. IR spectra of methanol ice exposed to UV photons at 12 K. The spectra are offset for clarity. IR assignments of species formed during photolysis are listed in Table 1.

In Figure 1, the large methanol peak at 1044 cm^{-1} decreased significantly as the UV fluence increased, confirming the photodestruction of methanol. Several IR features appeared as the UV fluence increased as well. Over the one-hour exposure, these features continually increased in absorbance. Figure 2 shows the spectrum of the methanol ice before and after photolysis in the $1400\text{--}800\text{ cm}^{-1}$ range to highlight IR features that arise primarily from larger organics. See Table 1 for a list of IR assignments.

Many of the features listed in Table 1 have more than one possible carrier and are indistinguishable without further studies, such as isotopic substitution for example. More products were identified upon ice warm-up, but it should be noted that this procedure cannot fully confirm all unique photoproducts that were present at 12 K.

3.2. Heating from 12 to 300 K

The photolyzed methanol ices were heated from 12 to 300 K, and IR spectra were collected every 10 K to monitor the sublimation of photoproducts and to understand the reactions that occurred during this warm-up process. No additional features were detected that were not present at 12 K, but several of them increased in peak absorbance. First, the broad peak at $\sim 3300\text{ cm}^{-1}$ (the O-H stretching region) increased in absorbance between 12 and 125 K. The absorptions of the O-H stretching region disappeared above 125 K, which is consistent with the sublimation of methanol. The absorbance increase observed could be due to radical-radical recombination that produced water and alcohols (e.g. ethanol), from the rapid crystallization of methanol when heated above $\sim 100\text{ K}$ (Luna et al. 2018), or **potentially the redeposition of gases within the chamber.**

Figure 3 shows the change in the IR spectrum as the ice was heated. The left panel shows the increase in the O-H stretch from 12 to 45 K, 45 to 85 K, and 85 to 125 K. After 125 K the absorbance decreased as the ice sublimated.

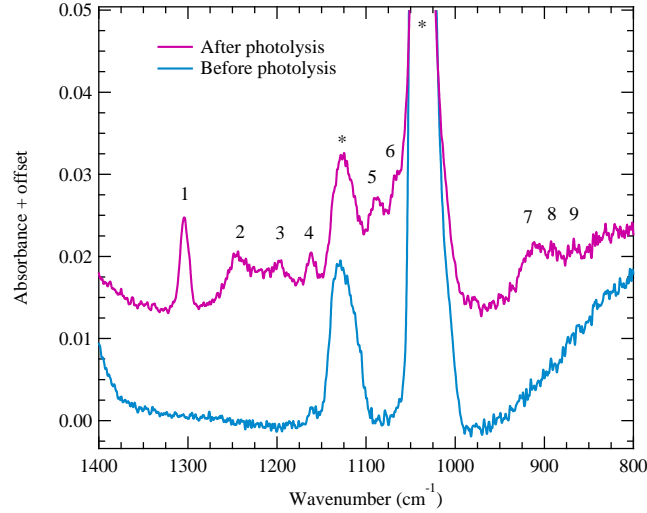


Figure 2. 1400-800 cm^{-1} IR spectrum of methanol ice at 12 K before (bottom) and after (top) UV photolysis for one hour. The numbers 1-9 label IR features that appeared after photolysis, and the vibrational transitions of methanol are labeled with asterisks. The nine IR features are assigned in Table 1 and include the bands listed from the methane peak at 1303 cm^{-1} to the ethylene glycol peak at 867 cm^{-1} .

Table 1. IR assignments in the spectrum of UV-photolyzed methanol ice at 12 K

Band Position (cm^{-1})	Chemical Formula	Chemical Name	Figure 2 Label	Reference
2341	CO_2	Carbon dioxide	-	1
2136	CO	Carbon monoxide	-	1
1722	H_2CO , CH_3CHO , HCOOCH_3	Formaldehyde, acetaldehyde, methyl formate	-	2, 3, 4
1303	CH_4	Methane	1	1
1245	H_2CO , CH_3OCH_3	Formaldehyde, dimethyl ether	2	2, 5
1197	CH_2OH	Hydroxymethyl radical	3	6
1162	HCOOCH_3 , CH_3OCH_3	Methyl formate, dimethyl ether	4	4, 5
1091	CH_3OCH_3 , $(\text{CH}_2\text{OH})_2$, $\text{CH}_3\text{CH}_2\text{OH}$	Dimethyl ether, ethylene glycol, ethanol	5	5, 7, 8
1060	$\text{CH}_3\text{CH}_2\text{OH}$	Ethanol	6	8
919	CH_3OCH_3	Dimethyl ether	7	5
910	HCOOCH_3	Methyl formate	7	4
887	$(\text{CH}_2\text{OH})_2$, $\text{CH}_3\text{CH}_2\text{OH}$	Ethylene glycol, ethanol	8	7, 8
867	$(\text{CH}_2\text{OH})_2$	Ethylene glycol	9	7

References—(1) Cruz-Diaz et al. (2016) (2) Gerakines et al. (1996), (3) Hudson & Moore (2000), (4) Modica & Palumbo (2010), (5) Hudson et al. (2020), (6) Öberg et al. (2009), (7) Hudson et al. (2005), (8) Hudson (2017).

205 The right panel shows the change in absorbance for several peaks from 1350 to 800 cm^{-1} (see Table 1). The features
 206 of methane (1303 cm^{-1}) and the hydroxymethyl radical (CH_2OH , 1197 cm^{-1}) decreased above 12 K. Increases in
 207 absorbance were observed at 1091, 887, and 867 cm^{-1} , due to both ethanol and ethylene glycol (which could not
 208 be distinguished with this technique). Since ethanol and ethylene glycol form from radical recombination reactions
 209 involving the hydroxymethyl radical, this behavior of their IR features suggests that some ethanol and ethylene glycol
 210 was produced during warm-up. The peaks at 1245, 1162, and 910 cm^{-1} , assigned to dimethyl ether and methyl formate,

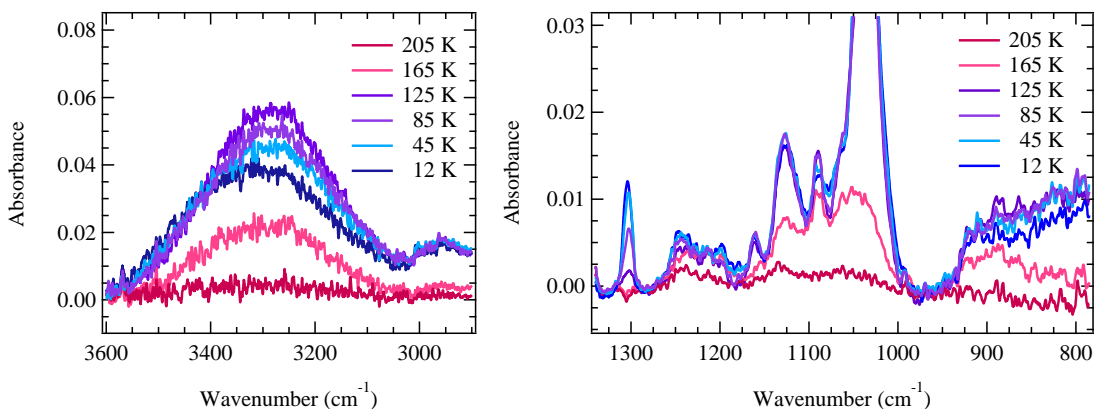


Figure 3. IR spectra of the UV photolyzed methanol ice warmed from 12 to 205 K. Left panel: 3600-2900 cm^{-1} . Right panel: 1350-800 cm^{-1} .

211 did not increase as the ice was heated. Both products are formed via radical recombination reactions involving the
 212 methoxy radical (CH_3O), and these peaks decreased rapidly after the ice was heated above 125 K.

213 Mass spectra were also collected from $m/z = 1$ to 65 daltons in 10 K increments as the ice was warmed. Temperature-
 214 programmed desorption (TPD) curves were constructed from these data for the m/z of potential photoproducts that
 215 were not detectable by the submillimeter spectrometer (see Section 3.3).

216 3.3. Gas-phase Composition at 300 K

217 The composition of the gases from the UV-photolyzed methanol ice, after warm-up to 300 K, was determined using
 218 submillimeter/far-IR spectroscopy. First, broadband spectra were collected that focused on the detection of two of
 219 the main photoproducts of methanol ice photolysis: carbon monoxide (CO) and formaldehyde (H_2CO). From these
 220 broadband spectra, various rotational transitions were detected and were used to identify more photoproducts. After
 221 those identifications were made, targeted searches were carried out to confirm those initial broadband detections and to
 222 search for even more products. All spectra presented in this section have been power corrected and the intensities are
 223 in units of voltage (mV) and/or temperature (K). Lastly, many of the center frequencies of the rotational transitions
 224 are labeled by dotted lines and with their respective quantum numbers as $J_{K_a',K_c'} - J_{K_a,K_c}$.

225 Broadband spectra were collected in the ranges of 758350-760130 MHz, 806500-812890 MHz, and 921470-92550 MHz
 226 (Figure 4). See Appendix A and Table A1 for the assignment of the 806500-812890 MHz spectrum. These spectral
 227 windows were selected initially to detect CO and H_2CO and contained the highest power in this high-frequency
 228 submillimeter region of the spectrometer (Band 9, 700-1000 GHz). Two peaks were detected for CO at 806651.81 and
 229 921799.83 MHz, and two peaks were detected for H_2CO at 812831.41 and 923587.96 MHz.

230 After initial identifications were made for several molecules, spectra were then collected for targeted transitions in
 231 order to improve signal-to-noise ratio and to search for products with weaker transitions in these spectral regions.
 232 These results as well as reported photoproducts from the literature were used to make targeted searches for more
 233 molecules. In the following paragraphs, the complex organic molecules (COMs), which we define as molecules that
 234 contain two or more C-atoms, detected in the gas phase after ice warm-up are reported in order of increasing molecular
 235 weight.

236 3.3.1. Ketene $\text{C}_2\text{H}_2\text{O}$

237 Five spectral lines were detected for ketene (also referred to as ethenone), the simplest member of the ketene group.
 238 Ketene has relatively intense features at submillimeter wavelengths and was first observed in the 806500-812890 MHz
 239 broadband spectrum. All five peaks are shown in Figure 5.

240 3.3.2. The $\text{C}_2\text{H}_4\text{O}$ Isomers Acetaldehyde, Ethylene Oxide, and Vinyl Alcohol

241 Acetaldehyde has been previously reported as a UV photoproduct of methanol ice (Abou Mrad et al. 2016;
 242 Paardekooper et al. 2016; Öberg et al. 2009), but to our knowledge ethylene oxide and vinyl alcohol have not. In
 243 this study, all three of the $\text{C}_2\text{H}_4\text{O}$ isomers were searched for and identified via detection of at least five unique rota-
 244 tional transitions.

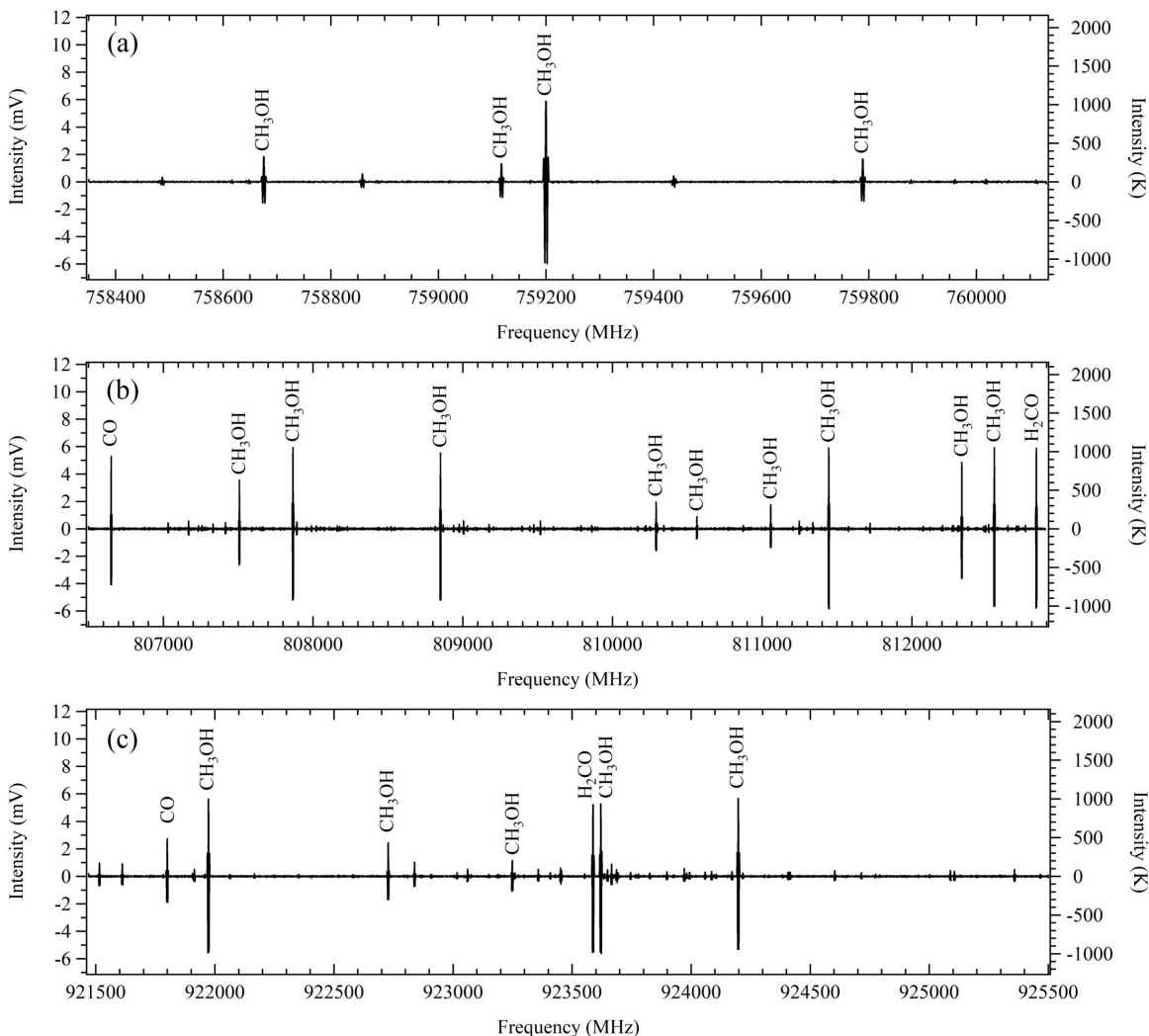


Figure 4. Broadband submillimeter/far-IR spectra at (a) 758350-760130 MHz, (b) 806500-812890 MHz, and (c) 921470-92550 MHz. Rotational transitions with an intensity greater than 1 mV are labeled with molecule name. Spectra were boxcar-smoothed with a window of 10 points to reduce noise.

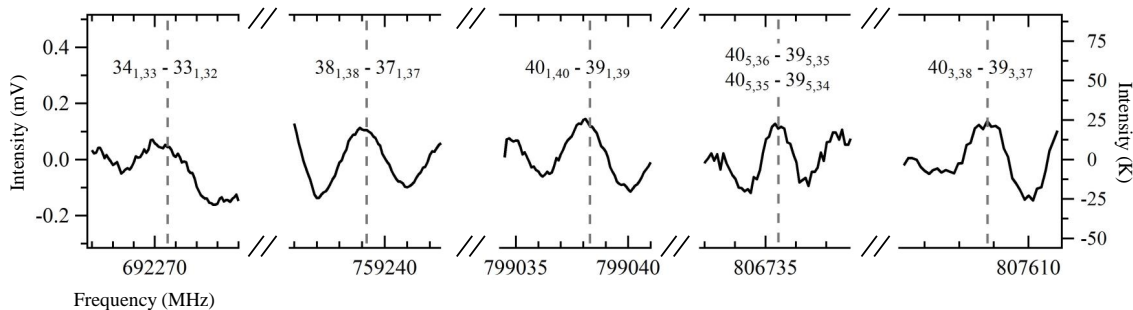


Figure 5. Five detections of ketene transitions including three peaks from the broadband scans and two additional targeted transitions. Rotational quantum numbers are labeled for each transition $J'_{Ka',Kc'} - J_{Ka,Kc}$.

Although several acetaldehyde detections were made in our broadband data, it initially was a complicated molecule to identify because many of the transition frequencies in the spectral catalog have very large uncertainties (≥ 10

247 MHz). However, we collected spectra of an acetaldehyde standard to confirm and identify all acetaldehyde peaks in
 248 the broadband data.

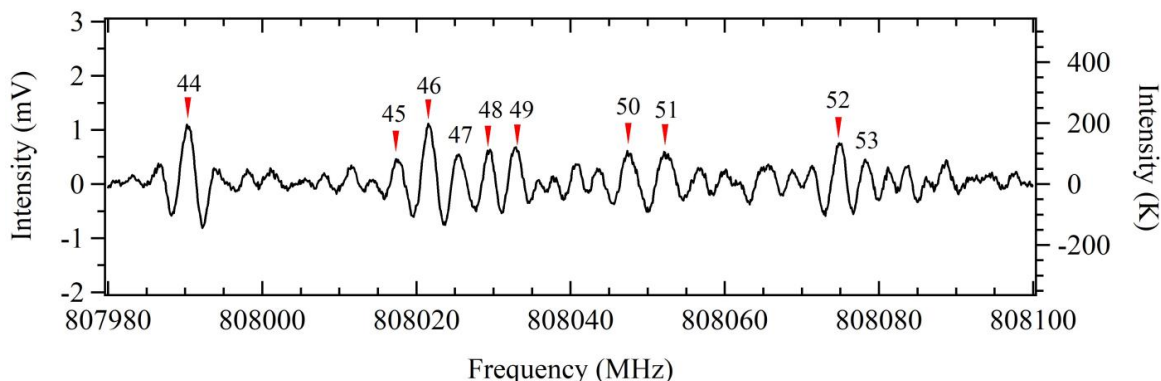


Figure 6. Eight acetaldehyde peaks from 807980 to 808100 MHz labeled with red arrows. The numbers correspond to Table A1. For reference, the standard deviation of the noise for this spectrum was 0.1 mV making $5\text{-}\sigma = 0.5$ mV.

249 A large portion of the detections for acetaldehyde were blended with neighboring peaks, and Figure 6 demonstrates
 250 how crowded these rotational spectra can be. Despite this, five peaks were uniquely resolved and were used for a
 251 rotational-diagram analysis to determine the temperature and density of the acetaldehyde gas present after warm-up
 252 (see Section 3.4).

253 Ethylene oxide has intense rotational features at high frequencies in the broadband scans, and a few transitions were
 254 detected that were not blended with other products. These features were then confirmed by collecting more spectral
 255 averages and searching for more transitions at other frequencies. In total, eight peaks were detected for *cis*-ethylene
 256 oxide and are shown in Figure 7.

257 The third $\text{C}_2\text{H}_4\text{O}$ isomer is vinyl alcohol, which is considerably less stable than acetaldehyde and ethylene oxide
 258 under standard laboratory conditions. It exists in two conformational structures: *syn* and *anti*. The submillimeter/far-
 259 IR spectrum of the *anti* conformation possesses significantly stronger absorption signals than the *syn* conformer. The
 260 rotational spectrum of vinyl alcohol, in either conformation, has only been predicted below 720 GHz. Therefore, it
 261 could not be identified in the broadband scans, but a targeted search was performed for five transitions of *anti*-vinyl
 262 alcohol which led to those shown in Figure 8.

263 3.3.3. The $\text{C}_2\text{H}_6\text{O}$ Isomers Ethanol and Dimethyl Ether

264 The two $\text{C}_2\text{H}_6\text{O}$ isomers ethanol and dimethyl ether have been reported previously as methanol ice photoproducts
 265 (Schneider et al. 2019; Paardekooper et al. 2016; Öberg et al. 2009). Both the *trans* and *gauche* forms of ethanol
 266 were prominent in the broadband spectra measured here. Figure 9 shows ten transitions that were detected for *trans*-
 267 ethanol. The *trans*-conformation is the most stable configuration, and its rotational transitions are more intense than
 268 those of the *gauche*-conformation.

269 It was not clear initially whether *gauche*-ethanol would be detected. After the notably significant abundance of *trans*-
 270 ethanol was observed, a search for *gauche*-ethanol was conducted, and nine non-blended detections were confirmed
 271 (Figure 10).

272 Searches were also conducted for the second $\text{C}_2\text{H}_6\text{O}$ isomer, dimethyl ether. Five absorption signals were detected
 273 in the broadband scans (Figure 11). The structure of dimethyl ether contains two methyl rotors which results in
 274 transitions to be split into four substates (*EE*, *EA*, *AA*, and *AE*). Therefore, the rotation diagram analysis required
 275 determination of the separate components of the peak areas for each of these blended transitions. The individual
 276 peak areas were found by first integrating the 2f line shape twice to convert it to a Gaussian line shape, and then
 277 fitting individual Gaussian peaks for the blended transitions using the multipeak fitting function within the IGOR Pro
 278 software package. The rotation diagram analysis results are presented in Section 3.4.

279 3.3.4. The $\text{C}_2\text{H}_4\text{O}_2$ Isomers Methyl Formate, Glycolaldehyde, and Acetic Acid

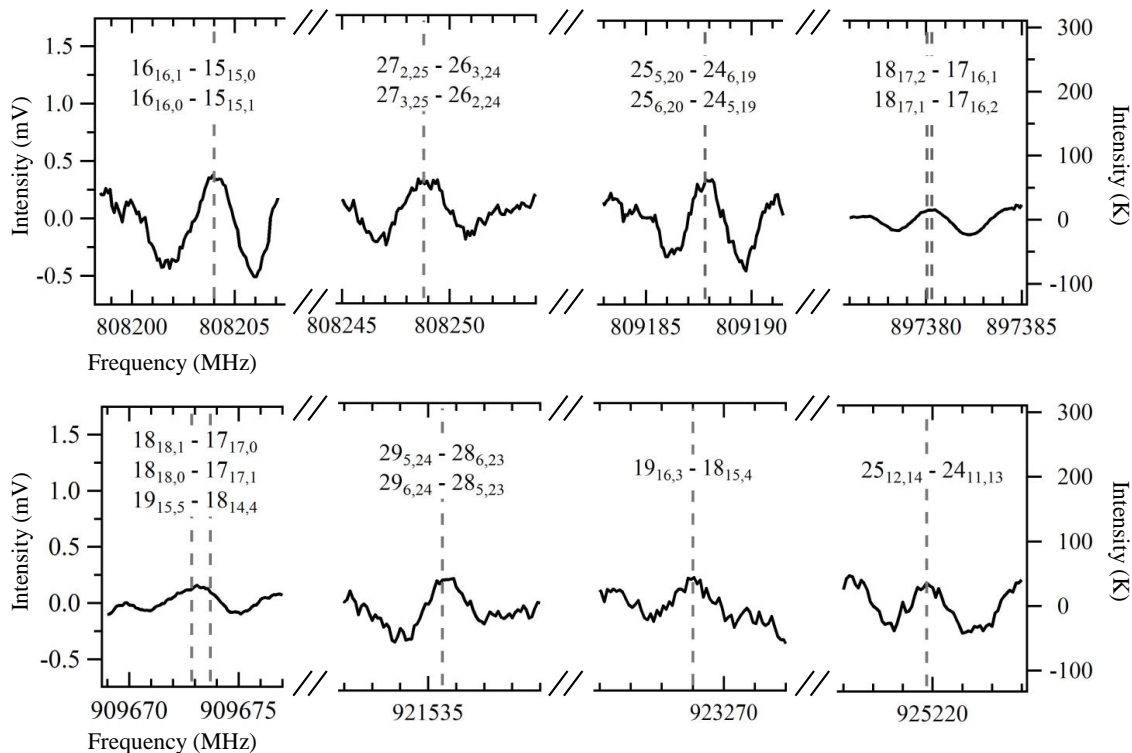


Figure 7. Eight detections of *cis*-ethylene oxide including six peaks in the broadband spectra and two targeted spectra. Rotational quantum numbers are labeled for each transition $J'_{Ka',Kc'} - J_{Ka,Kc}$.

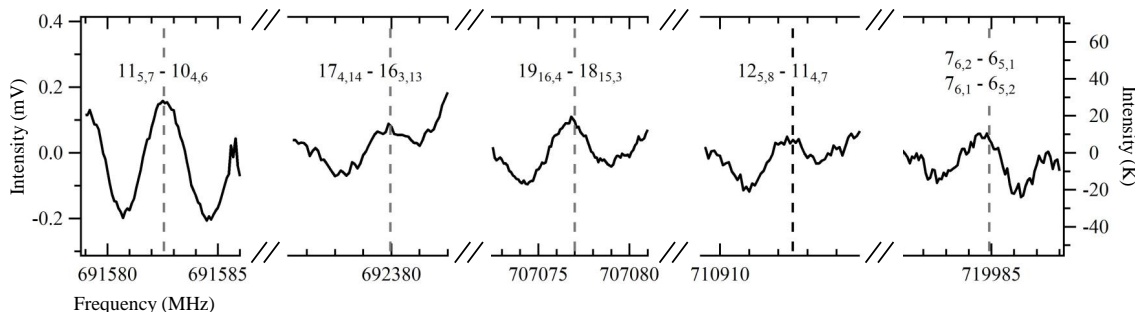


Figure 8. Five detections of *anti*-vinyl alcohol transitions from targeted submillimeter searches. Rotational quantum numbers are labeled for each transition $J'_{Ka',Kc'} - J_{Ka,Kc}$.

280 The $C_2H_4O_2$ isomers have been reported previously as UV photoproducts of methanol ices (Öberg et al. 2009), but
 281 they cannot be uniquely identified in either IR or mass spectra because their signatures are too similar. Acetic acid
 282 and methyl formate have been reported as UV photoproducts of methanol ice by gas chromatography coupled with
 283 mass spectrometry, but glycolaldehyde could not be detected due to the analytical setup (Abou Mrad et al. 2016).
 284 These three isomers can be distinguished and quantified with the techniques implemented in this study, and searches
 285 for all three were successfully conducted.

286 Methyl formate has two conformations: *cis* and *trans*. The most stable conformation is *cis*, and six transitions were
 287 detected for *cis*-methyl formate from targeted searches (Figure 12). We were not able to search for the *trans*-conformer
 288 because the submillimeter spectrum of *trans*-methyl formate has yet to be measured experimentally.

289 Nine transitions were detected for glycolaldehyde (Figure 13). Unlike methyl formate, glycolaldehyde has significantly
 290 stronger transitions within the broadband scan frequencies arising from its stronger dipole moment and lack of internal
 291 rotation.

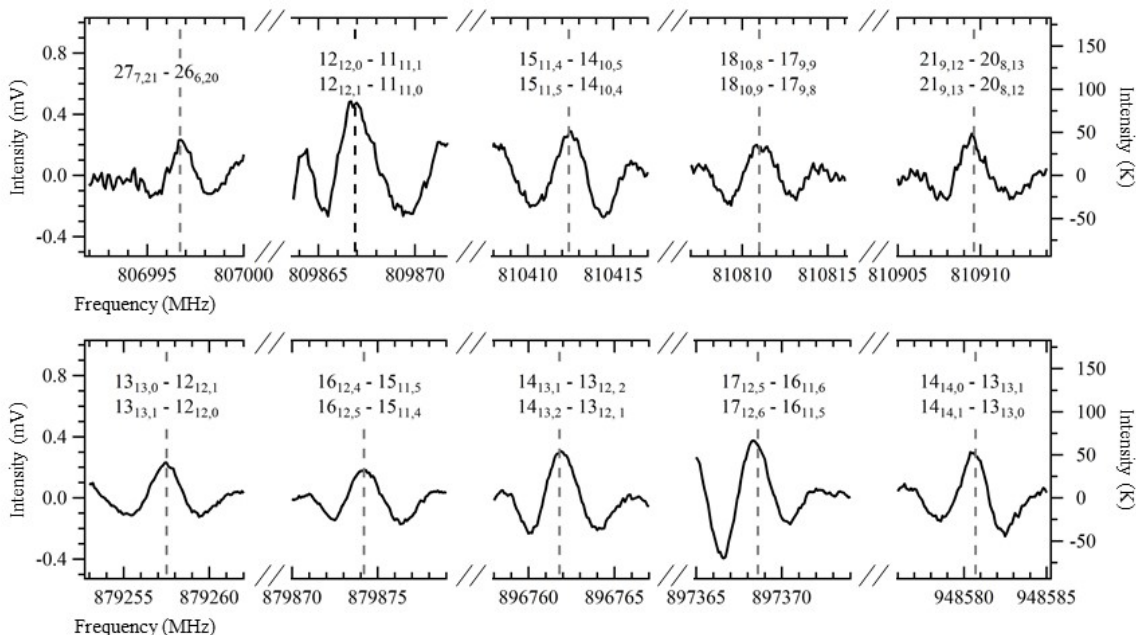


Figure 9. Ten detections of *trans*-ethanol transitions including five peaks from the 806500-812890 MHz scan (top row) and five separate targeted transitions (bottom row). Rotational quantum numbers are labeled for each transition $J'_{K_a',K_c'} - J_{K_a,K_c}$.

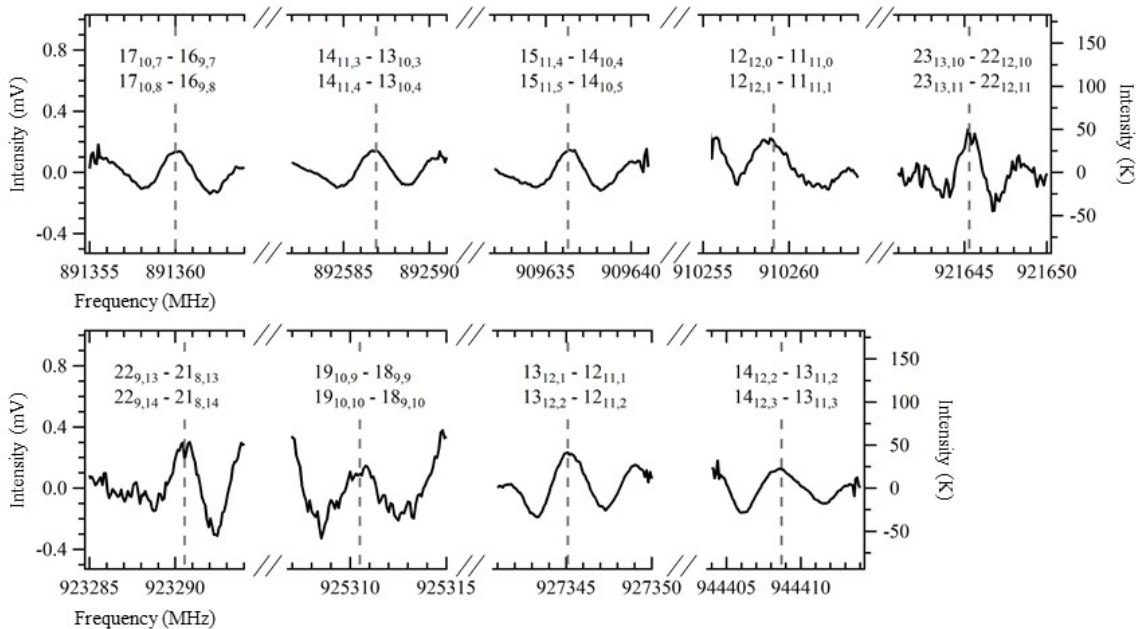


Figure 10. Nine detections of *gauche*-ethanol transitions including three peaks detected in the 921470-92550 MHz scan and six peaks from separate targeted searches. Rotational quantum numbers are labeled for each transition $J'_{K_a',K_c'} - J_{K_a,K_c}$.

292 Searches were also conducted for the third $C_2H_4O_2$ isomer, acetic acid. Four peaks were detected near the center
 293 frequencies of acetic acid at levels $\geq 5\sigma$, but three other peaks of similar intensity were not detected. The most intense
 294 transitions of acetic acid are even lower in intensity than those of methyl formate and significantly lower in intensity
 295 than those of glycolaldehyde. Consequently, the detection limit of acetic acid is higher than the detection limits of
 296 the other two isomers. A rotation diagram analysis was performed for the four detections, but gave unrealistic values

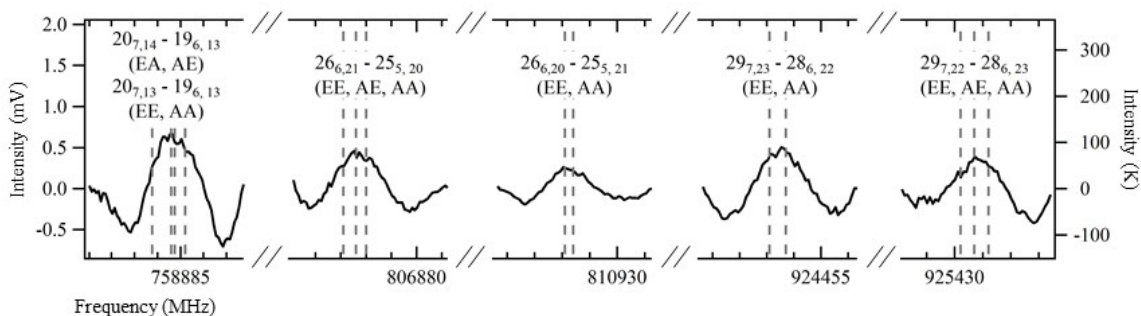


Figure 11. Five detections of dimethyl ether in the broadband scans. Rotational quantum numbers are labeled for each transition $J'_{Ka',Kc'} - J_{Ka,Kc}$.

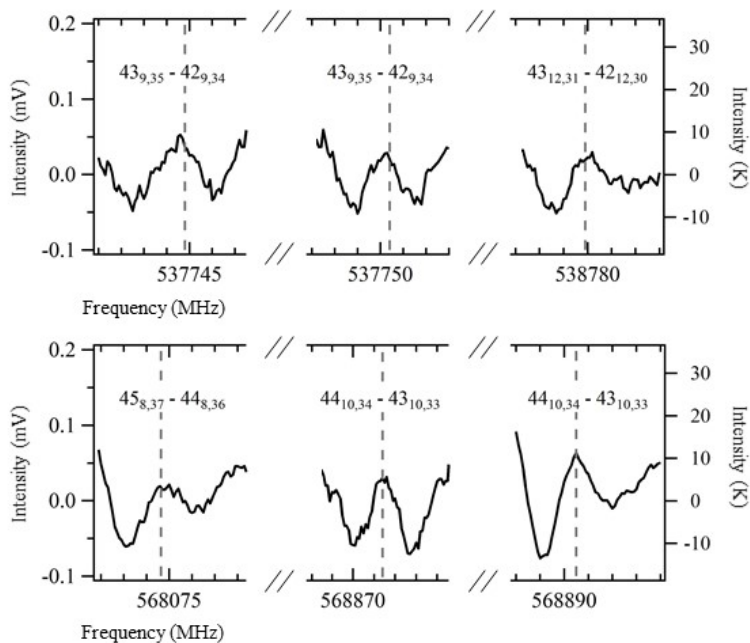


Figure 12. Six detections of *cis*-methyl formate from targeted searches. Rotational quantum numbers are labeled for each transition $J'_{Ka',Kc'} - J_{Ka,Kc}$.

297 for temperature and density. Therefore, acetic acid was not confirmed as a photoproduct. If it was present, then its
 298 concentration was below the detection limit of the spectrometer.

299 3.3.5. The $C_2H_6O_2$ Isomers Ethylene Glycol and Methoxymethanol

300 Two $C_2H_6O_2$ isomers, ethylene glycol and methoxymethanol, have both been reported previously as UV-
 301 photoproducts of methanol ice and were therefore considered in this study (Schneider et al. 2019; Paardekooper
 302 et al. 2016). Furthermore, IR features that aligned with those of ethylene glycol were present in the FTIR spectra at
 303 12 K (see Figure 2 and Table 1). The most stable conformation of ethylene glycol, aGa' , was targeted based on the
 304 recent submillimeter assignment published by Melosso et al. (2020). Searches for nine transitions were conducted in
 305 this study. Out of those nine transitions, only two clear detections were made. Four more peaks that were targeted
 306 showed significant blending with neighboring photoproduct transitions and were not individually resolved. The remain-
 307 ing three searches for transitions of similar intensities resulted in non-detections. Therefore, ethylene glycol could
 308 not be confirmed as a photoproduct in these experiments.

309 Methoxymethanol has a straightforward formation pathway from the recombination of the methoxy and hydroxymethyl
 310 radicals. Unfortunately, the detection limit for methoxymethanol at submillimeter wavelengths is quite high,
 311 and it was not detected in these experiments. Both $C_2H_6O_2$ isomers were searched for in the mass spectral data

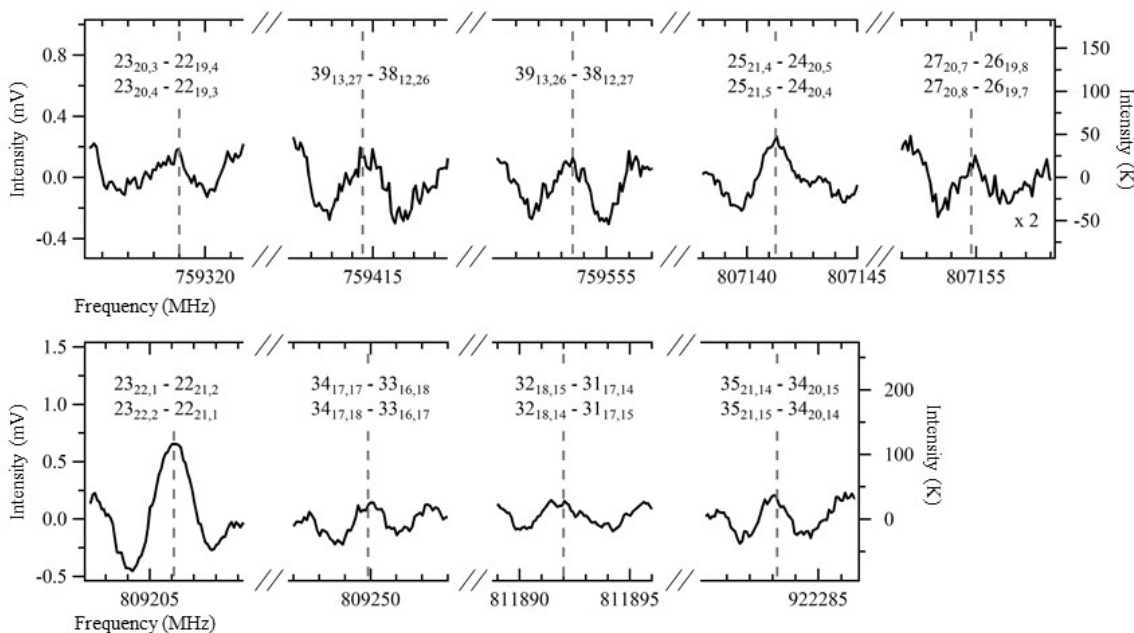


Figure 13. Nine detections of glycolaldehyde in the broadband submillimeter spectra. The intensity of the peak at 807155 MHz was multiplied by two for visibility. Rotational quantum numbers are labeled for each transition $J'_{Ka',Kc'} - J_{Ka,Kc}$.

from TPD curves of $m/z = 61$ and 62 . There were no signals present at these m/z at the appropriate desorption temperatures, ~ 155 K for methoxymethanol (Schneider et al. 2019) and ~ 185 K for ethylene glycol (Öberg et al. 2009). The lack of production of these two COMs may be due to the differences in ice temperature during photolysis. The studies conducted by Schneider et al. and Öberg et al. reported one or both of these products at photolysis temperatures of 90 and 70 K, respectively.

3.3.6. Acetone ($CH_3)_2CO$

The molecule with the largest number of atoms that was detected in this study was acetone. The submillimeter spectrum of acetone has relatively weak absorption signals (due to its two methyl rotors that cause torsional splitting into four substates), resulting in a relatively high detection limit. Acetone has been reported by others as a radiation product of methanol ice (Abou Mrad et al. 2016; Henderson & Gudipati 2015; Öberg et al. 2009) and controversially as a non-product of proton-irradiated $H_2O + CH_3OH$ ice (Hudson & Moore 2000). Three non-blended detections were made for acetone in this study (Figure 14) while other transitions for which we searched were overwhelmed by intense, neighboring methanol transitions.

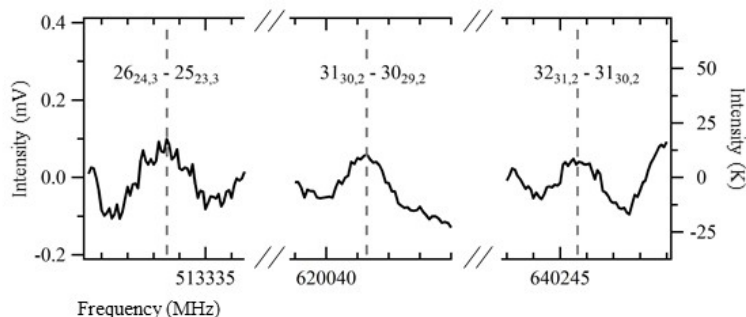


Figure 14. Three detections of acetone transitions from targeted searches. Rotational quantum numbers are labeled for each transition $J'_{Ka',Kc'} - J_{Ka,Kc}$.

3.4. Rotation Diagram Analysis Procedure and Results

326 A rotation diagram analysis can be used to determine the rotational temperatures and densities of molecules from the
 327 integrated intensities of their respective rotational transitions. This process is also commonly referred to as Boltzmann
 328 analysis or population diagram analysis, which is described (along with the underlying physics) by Goldsmith & Langer
 329 (1999) and references therein. This technique has been widely used by astronomers for determining temperature and
 330 density of molecules detected in observational data, and Laas et al. (2013) showed that it also could be adapted for
 331 use in laboratory absorption spectroscopy studies like those performed here. The application of the rotation diagram
 332 approach by Laas et al. only considered optically thin transitions and cannot be used to quantify the observed products
 333 in our experiments. In the present work, the Laas et al. technique was adapted to include the full treatment as laid
 334 forth by Goldsmith & Langer using a Python3 program.

335 The rotation diagram analysis utilizes the following equation

$$\ln \left(\frac{8\pi k v^2 W}{hc^3 A_{ul} g_u} \right) = \ln \left(\frac{N}{Z} \right) - \frac{E_u}{kT} - \ln(C_\tau), \quad (1)$$

336 where W is the integrated intensity⁵, v is the center frequency of the transition, A_{ul} is the Einstein A-coefficient for
 337 the transition, g_u is the upper-state degeneracy, N is the total column density, Z is the partition function (i.e., the
 338 sum of densities of states), E_u is the upper-state energy, T is the rotational temperature, C_τ is an optical depth (τ)
 339 correction factor, k is Boltzmann's constant, h is Planck's constant, and c is the speed of light. For simplicity, we
 340 define γ to be equal to $8\pi k v^2 / hc^3 A_{ul}$. The best-fitting slope and y-intercept of a plot of $\ln(\gamma W C_\tau)$ vs. E_u can then
 341 be used to determine T and N according to equation 1.

342 The optical depth correction factor is given by

$$C_\tau = \frac{\tau}{1 - e^{-\tau}} \quad (2)$$

$$\tau = \frac{h}{\Delta v} N_u B_{ul} \left(e^{\frac{h\nu}{kT}} - 1 \right) \quad (3)$$

$$N_u = \frac{N}{Z} g_u e^{-\frac{E_u}{kT}} \quad (4)$$

343 where Δv is the FWHM of the peak, N_u is the upper-state density, and B_{ul} is the Einstein B-coefficient calculated
 344 according to

$$B_{ul} = \frac{A_{ul} c^3}{8\pi h v^3}, \quad (5)$$

345 and for laboratory spectra, as presented herein, the Einstein A-coefficient is calculated from

$$A_{ul} = (2.7964 \times 10^{-16}) I_{cat}(T) v^2 \left(\frac{Z}{g_u} \right) \left(e^{-\frac{E_l}{kT}} - e^{-\frac{E_u}{kT}} \right)^{-1} \quad (6)$$

346 where $I_{cat}(T)$ is the temperature dependent catalog intensity value and E_l is the lower-state energy. The values needed
 347 for all calculations (i.e., $I_{cat}(T)$, E_l , E_u , g_u , Z) can be found in the spectral catalog files for the molecule(s) of interest
 348 (e.g., JPL and/or CDMS catalogs).

349 A few conversions are needed to adapt the analysis for use with the laboratory spectra in this work. First, the peak
 350 intensity is converted from volts to Kelvin. This was achieved by converting the voltage output from the detector to
 351 Watts by dividing the voltage by the detector's optical responsivity (170 kV W⁻¹). The power was then converted to
 352 Kelvin by dividing power by the product of the detector bandwidth with Boltzmann's constant. Secondly, the peak
 353 width (Δv) refers to the FWHM of a Gaussian line shape in velocity units. Due to the 2f line shapes, a FWHM cannot
 354 be directly determined from the raw spectra, but it can be calculated because the line shape is simply the second
 355 derivative of a Gaussian line shape. Therefore, the respective peak widths are

⁵ The integrated intensity, W , was determined using the composite Simpson's rule. The integration range was the frequency range that covered the 2f line shape, and the negative area of the side lobes was added to the positive area of the center peak.

$$w_{2f} = 2\sqrt{3}w \quad (7)$$

$$w_{FWHM} = 2\sqrt{2\ln(2)}w \quad (8)$$

where w_{2f} is the peak width of the 2f line shape between the side lobe minima, w is a line width factor, and w_{FWHM} is the FWHM of the Gaussian line shape. Next, the line width units were converted to velocity units by dividing w_{FWHM} by the center frequency, ν , and multiplying by the speed of light, c .

The uncertainty of $\ln(\gamma WC_\tau)$ (i.e., the y-axis error bars) was determined based on the propagation of errors that considered the uncertainties of the peak area, center frequency, and the Einstein A-coefficient, while the uncertainty of the Einstein A-coefficient itself considered the uncertainties of center frequency and peak intensity. The rotation diagrams for methanol and the reported complex organic photoproducts are presented in Figure 15, which are labeled with the molecule’s name and the calculated rotational temperature and gas density. A summary of the results can be found in Table 2 which includes the calculated temperatures, calculated densities, and abundance ratios of product normalized to methanol. See Appendix B and Table B1 for the parameters used for the rotation diagram analysis of each molecule.

Table 2. Summary of Rotation Diagram Analyses

Molecule	Temperature (K)	Density (10^{11} molec. cm^{-3})	Abundance Ratio
Methanol	270 ± 17	2800 ± 440	1.0000
Ketene	280 ± 42	2 ± 1.2	0.0007
Acetaldehyde	220 ± 14	160 ± 57	0.0571
Ethylene oxide	300 ± 27	3.7 ± 0.6	0.0013
<i>anti</i> -Vinyl alcohol	290 ± 42	2.6 ± 0.41	0.0009
Ethanol	140 ± 18	70 ± 18	0.0250
Dimethyl ether	170 ± 68	200 ± 180	0.0714
Methyl formate	160 ± 10	40 ± 11	0.0143
Glycolaldehyde	310 ± 42	13 ± 3.2	0.0046
Acetone	230 ± 24	50 ± 11	0.0179

NOTE—Abundance ratios are normalized to methanol. **The methanol gas density includes non-irradiated methanol desorbed from the substrate, the cryostat shaft, and the chamber walls and any methanol that was reformed during the ice warm-up.**

Before the experiments were conducted, it was unclear whether the rotational temperatures would reflect room/chamber temperature (~ 298 K) or if they would be related to the volatilities of the individual molecules. The former case was observed, within experimental error, for four products: ketene, ethylene oxide, *anti*-vinyl alcohol, and glycolaldehyde. In fact, glycolaldehyde was the warmest product at 310 ± 42 K. The second-highest temperature belonged to ethylene oxide. Glycolaldehyde and ethylene oxide are known to sublime rapidly at temperatures more than 100 K colder than their observed rotational temperatures. The coldest molecule was ethanol at 140 ± 18 K, followed by its structural isomer dimethyl ether at 170 ± 68 K. This rotational temperature agrees well with ethanol’s known volatility, while the rotational temperature of dimethyl ether, 170 ± 68 K, was significantly higher than would be predicted based on volatility alone. Considering structural isomers, the rotational temperatures of ethylene oxide and *anti*-vinyl alcohol were within 10 K. The third $\text{C}_2\text{H}_4\text{O}$ isomer, acetaldehyde, had a much lower rotational temperature. The rotational temperatures of the $\text{C}_2\text{H}_6\text{O}$ isomers, ethanol and dimethyl ether, had a difference of 30 K with dimethyl ether being the warmer isomer. Lastly, the $\text{C}_2\text{H}_4\text{O}_2$ isomers, methyl formate and glycolaldehyde, had significantly different temperatures. Glycolaldehyde was almost twice as warm as methyl formate. No clear overall

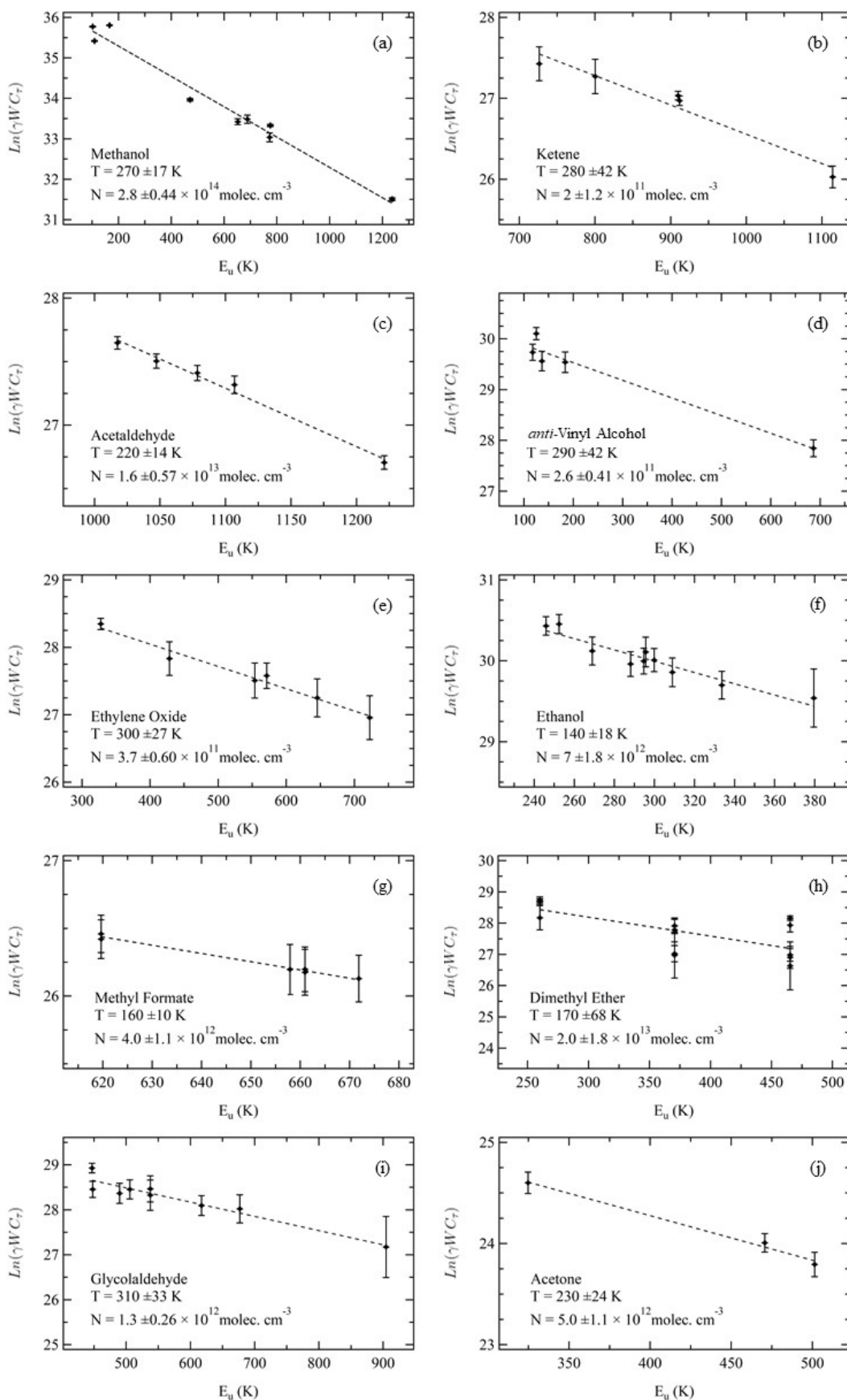


Figure 15. Rotation diagrams of (a) methanol, (b) ketene, (c) acetaldehyde, (d) ethylene oxide, (e) *anti*-vinyl alcohol, (f) ethanol, (g) dimethyl ether, (h) methyl formate, (i) glycolaldehyde, (j) acetone. Errors are described in Section 3.4.

trends can be deduced from the temperatures derived in this work and further studies need to be conducted to reveal more information about rotational temperatures of species desorbed from ices.

The three most-abundant COMs were dimethyl ether, acetaldehyde, and ethanol, in order of decreasing abundance. Acetaldehyde was the most abundant C_2H_4O isomer and *anti*-vinyl alcohol was the least abundant, which follows observational trends (see Section 4.1.1). Dimethyl ether was the most abundant C_2H_6O isomer above ethanol. Lastly, methyl formate was the most abundant $C_2H_4O_2$ isomer followed by glycolaldehyde which also matches well with observations (see Section 4.1.1). The three least-abundant products that were within the detection limits of the spectrometer were ketene, *anti*-vinyl alcohol, and ethylene oxide. This was not a surprise considering these three species require multi-step formation mechanisms beyond radical-radical recombination reactions (e.g., hydrogen abstraction(s) from ethanol). The following section contains a more in-depth discussion of the abundance ratios found in this study.

4. DISCUSSION

4.1. *The Benefits of Utilizing Submillimeter/far-IR Spectroscopy to Identify **Products of Sublimated Astrophysical Ices***

Submillimeter/far-IR spectroscopy is a powerful technique for identifying components of complex gas mixtures. The three main benefits that submillimeter/far-IR spectroscopy provides for laboratory ice experiments are (1) the direct comparison of laboratory spectra with submillimeter/far-IR spectra collected via telescopes, (2) the straightforward identification of structural isomers, conformers, and isotopologues, and (3) experimental quantification of uniquely identified COMs to compare to astrochemical models of the ISM and planetary atmospheres. **“A few limitations should be noted along with the benefits of this technique. Any gas-phase experiment within a vacuum chamber must deal with interactions with the chamber walls: (1) the detected gas densities are affected by adsorption onto the walls, and (2) the chamber walls can act as a catalytic surface for reactions that can modify the gas composition. It also should be noted that the species detected via submillimeter/far-IR spectroscopy cannot be directly distinguished as ice-phase photolysis products. The experiment focused on products detected after the warm-up of a photolyzed methanol ice. Despite these limitations, which apply to all laboratory studies of gases sublimated from ice analogs, rotational spectroscopy remains a very powerful tool in the identification of products of these photolyzed ices.”**

4.1.1. *Direct Comparison to Submillimeter/Far-IR Telescope Data*

The spectrometer that was built for this experiment covers the same regions of the electromagnetic spectrum as several millimeter/submillimeter/far-IR telescopes (e.g., ALMA, SOFIA, NOEMA, *Herschel*/HIFI). In Figure 16 we demonstrate how the laboratory spectra of gases desorbed from ice can be compared to observational surveys such as that of Orion Kleinmann-Low (Orion-KL) collected with the HIFI instrument on the *Herschel Space Observatory*.

The red observational spectra in Figure 16 contain several transitions that overlap with the blue laboratory spectra of the gases desorbed from the UV-photolyzed methanol ice. Five emission features are labeled with their assigned molecules including methanol ($^{12}CH_3OH$ and the less abundant isotopologue $^{13}CH_3OH$), carbon monoxide (CO), dimethyl ether (CH_3OCH_3), and formaldehyde (H_2CO). The majority of the intense overlapping transitions present in Figure 16 were from $^{12}CH_3OH$. The agreement between these spectra demonstrates how laboratory ice experiments can be used to model formation mechanisms and physical parameters (e.g., temperature and density) of species detected in star-forming regions, such as Orion-KL, and other astrophysical/planetary environments.

4.1.2. *Detection and Quantification of Structural Isomers, Conformational Isomers, and Isotopologues*

The identification of structural isomers, conformational isomers (conformers), and isotopologues detected in a single gas mixture is straightforward when utilizing submillimeter/far-IR spectroscopy as the main detection method, and this study has demonstrated the unique direct detections of structural isomers, conformers, and isotopologues that were desorbed from a UV-photolyzed methanol ice. The structural isomers that were detected included three C_2H_4O isomers (acetaldehyde, ethylene oxide, and vinyl alcohol), two C_2H_6O isomers (ethanol and dimethyl ether), and two $C_2H_4O_2$ isomers (methyl formate and glycolaldehyde). The detection of the *trans* and *gauche*-conformers of ethanol demonstrated the ability to distinguish a single chemical component in two different conformations. Lastly, $^{13}CH_3OH$, the rarer isotopologue of methanol, was detected in the broadband spectra showing the capability for isotopologue detection. None of these isomers could be distinguished using mass spectrometry alone in the desorbed gas sample.

Not only does rotational spectroscopy provide an in-situ measurement featuring the unique rotational fingerprints of the molecules in a given gas mixture, those components can also be quantified in the sample directly through a

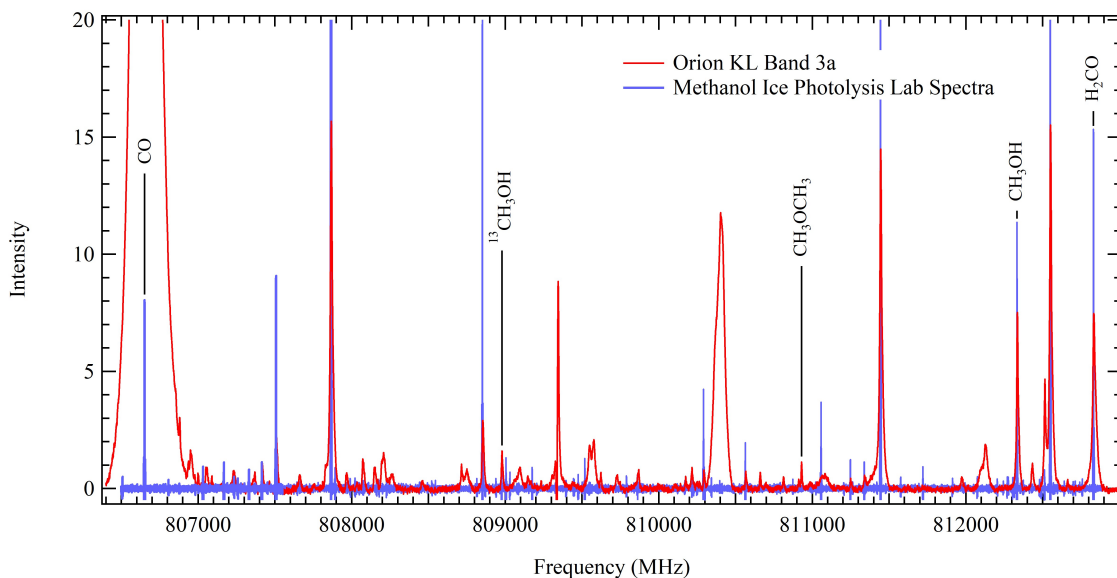


Figure 16. Overlaid spectra of the 806500-812890 MHz laboratory scan (blue) and a HIFI band 3a survey of Orion-KL (red). The intensities of the laboratory spectra were scaled down by three orders of magnitude for visual comparison. The Orion-KL spectral data were downloaded from the *Herschel* Science Archive and were first published by [Crockett et al. \(2014\)](#).

430 rotation diagram analysis without the need for further chemical separation or manipulation. The quantification of
 431 structural isomers, conformers, and/or isotopologues can even be achieved from a single spectrum. In this study,
 432 unstable species such as the hydroxymethyl (CH_2OH) and methoxy (CH_3O) radicals are not present after warm-up
 433 because they immediately recombine to form stable products. However, future studies will aim to determine the yields
 434 of unstable products that photodesorb from the ice surface at low temperatures (10-20 K) such as those found in
 435 various astrophysical environments such as cold dense clouds.

4.2. Methanol Branching Ratio Implications

436
 437 The photodissociation branching ratios of methanol are still unknown and are key to understanding COM formation
 438 on and within icy objects. Nonetheless, a few assumptions can be inferred from the relative abundances of the complex
 439 organics detected in this study. First, the most abundant product was dimethyl ether, CH_3OCH_3 , which may form
 440 from the radical-radical recombination of $\text{CH}_3 + \text{OCH}_3$, while its structural isomer, ethanol $\text{CH}_3\text{CH}_2\text{OH}$, likely forms
 441 from the radical-radical recombination of $\text{CH}_3 + \text{CH}_2\text{OH}$. Dimethyl ether had a much higher density than ethanol
 442 after ice warm-up, which implies that the $\text{H} + \text{CH}_3\text{O}$ radicals are formed in larger quantity than the $\text{H} + \text{CH}_2\text{OH}$
 443 radicals. The larger abundance of methyl formate (HCOOCH_3) versus glycolaldehyde (HOCH_2CHO) provides further
 444 evidence for this claim as methyl formate requires the CH_3O radical and glycolaldehyde requires the CH_2OH radical for
 445 formation. Even more evidence for CH_3O being the dominant methanol photoproduct is provided by the non-detection
 446 of ethylene glycol, $(\text{CH}_2\text{OH})_2$, which requires two CH_2OH radicals for formation. The computational study by [Laas
 447 et al. \(2011\)](#) showed the dependence of the $\text{C}_2\text{H}_4\text{O}_2$ isomer abundances on methanol ice photolysis branching ratios.
 448 Their results showed that to reproduce methyl formate abundances detected in Sagittarius B2(N), the $\text{H} + \text{CH}_3\text{O}$
 449 pathway must be favored over the $\text{H} + \text{CH}_2\text{OH}$ pathway, consistent with the findings of this work. Furthermore, the
 450 branching ratios that had the worst agreement with the observed abundances of methyl formate, glycolaldehyde, and
 451 acetic acid were those which favored the $\text{H} + \text{CH}_2\text{OH}$ pathway. The details of these reaction mechanisms are still
 452 a work in progress and will require additional experiments with isotopic labeling and confirmation of radicals from
 453 sublimation. Although the results in this study seem to support theoretical claims, this is in contradiction to the
 454 previous experimental study by [Öberg et al. \(2009\)](#) which determined the formation of $\text{H} + \text{CH}_2\text{OH}$ to be five times
 455 that of $\text{H} + \text{CH}_3\text{O}$. This previous experimental work relied on IR spectra of the ices and mass spectrometric analysis
 456 of the gas phase material during warm-up. Further studies both experimentally and theoretically are needed to verify
 457 the actual mechanisms at work. Regardless, this highlights the complementary strength brought to laboratory ice
 458 experiments by combining standard techniques with rotational spectroscopy.

4.3. Astrophysical Implications

All products reported herein originated from the UV photolysis **and subsequent warm-up** of a methanol ice. Those products included carbon monoxide, carbon dioxide (detected by FTIR spectroscopy), methane (detected by FTIR spectroscopy), formaldehyde, ketene, acetaldehyde, ethylene oxide, vinyl alcohol, ethanol, dimethyl ether, methyl formate, glycolaldehyde, and acetone. **To our knowledge, this is the first study that reports ketene, ethylene oxide, and vinyl alcohol as products of a methanol ice photolysis and sublimation experiment.** The production of these species should therefore be considered in computational astrochemical models of star formation and planetary atmospheres. Ketene has been reported previously by Maity et al. (2015) as a product from ion-processing of methanol ice, and vinyl alcohol was reported as a tentative detection in the same study. Future studies are required to determine probable formation mechanisms for these three species from the UV-photolysis of methanol.

The abundance ratios of the detected photoproducts with respect to methanol were compared to those detected in a high-mass protostar Orion-KL (Tercero et al. 2018), low-mass protostar IRAS 16293-2422(B) (Drozdovskaya et al. 2019), Sagittarius B2 (N) (Belloche et al. 2013), comet C/2014 Q2 (Lovejoy), hereafter Lovejoy, (Biver & Bockelée-Morvan 2019), and comet 67P/Churyumov-Gerasimenko, hereafter 67P/CG (Rubin et al. 2019b). Several trends were noticed between these abundance ratios in the various astronomical sources. Figure 17 shows abundance ratios of ethylene oxide, ethanol, dimethyl ether, methyl formate, glycolaldehyde, and acetone normalized to methanol as detected in Orion-KL in three different regions. The methyl formate peak (MF peak), ethanol peak (ET peak), and ethylene glycol peak (EG peak) regions were described and mapped by Tercero et al. (2018). The MF peak is located in the compact ridge and the ET and EG peaks are located closer to the hot core. The abundance ratios of these three regions were similar across all molecules. The laboratory results from this study are compared to these observational findings and are shown in gray in Figure 17. The abundance ratios from this study appear to be most similar to the EG peak abundances, thus simulate the chemistry occurring closer to the hot core where thermal reactions play a large role, and are less similar to the compact ridge where it is colder. The laboratory results over-produced glycolaldehyde and acetone, and under-produced methyl formate. There are various details that can be further studied to help explain this, but most likely there is inconsistency for these species due to ice composition, photolysis timescales, and other energetic processes that were not considered in this study. Further experiments are required to constrain these details, though this initial work is very intriguing.

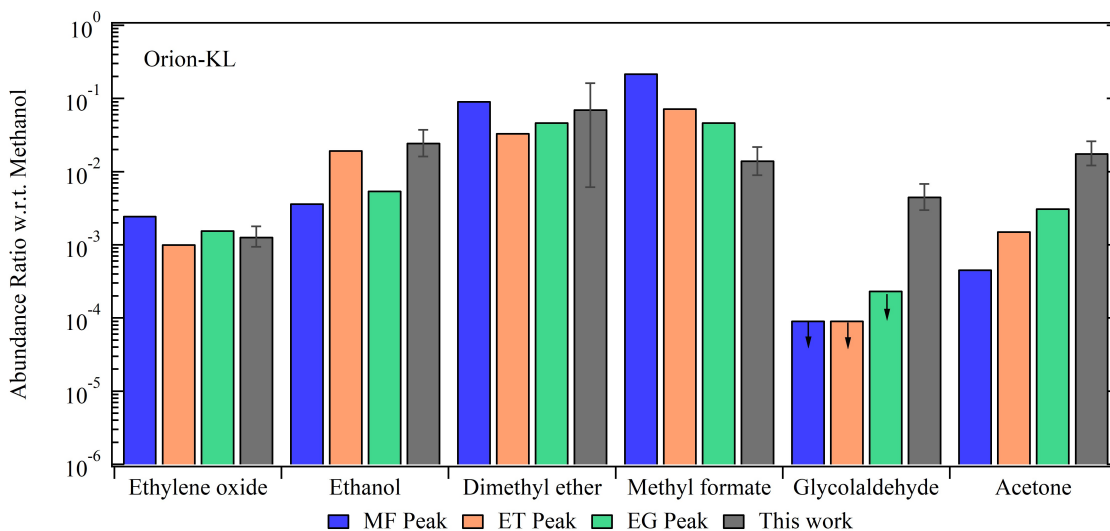


Figure 17. Abundance ratios of COMs relative to methanol as detected toward the high-mass protostar Orion-KL in three regions (MF peak, ET peak, and EG peak) compared to the laboratory results from this study. Observations from Tercero et al. (2018).

Figure 18 shows the abundance ratios of ketene, acetaldehyde, ethylene oxide, vinyl alcohol, ethanol, dimethyl ether, methyl formate, glycolaldehyde, and acetone normalized to methanol as detected in high-mass protostar Orion-KL (EG peak), protocluster Sagittarius B2(N), and low-mass protostar IRAS 16293-2422(B). The laboratory abundance

489 ratios from this work are shown in gray. Overall, the laboratory results appear most similar to the abundance ratios
 490 found in the low-mass protostar IRAS 16293-2422(B). This could be because the warm-up rate and UV fluence of these
 491 experiments better models a low-mass protostar than a high-mass protostar. Secondly, there are several gas-phase
 492 destruction pathways that further alter the abundances during the longer warm-up timescales of high-mass protostars.
 493 For example, the cosmic ray ionization rates (Bonfand et al. 2019) are likely an important factor that is not included
 494 in the current study.

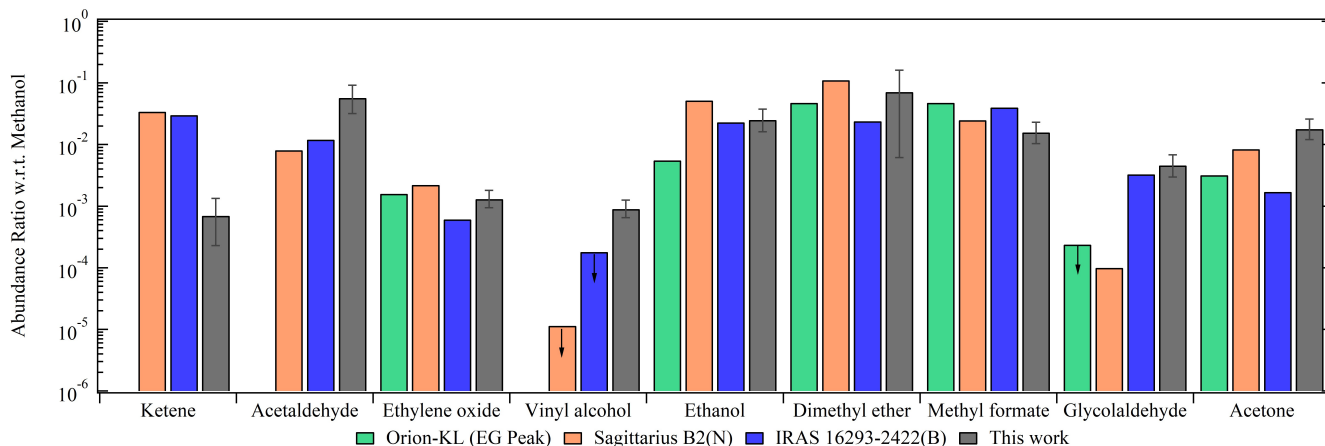


Figure 18. Abundance ratios of COMs relative to methanol as detected towards hot cores Orion-KL (EG peak), Sagittarius B2(N), IRAS 16293-2422(B) compared to the laboratory results from this study. Observations from Tercero et al. (2018); Belloche et al. (2013), and Drozdovskaya et al. (2019). Arrows denote upper limit detections.

495 A comparison of the abundance ratios for acetaldehyde, ethanol, methyl formate, and glycolaldehyde as detected in
 496 Comet Lovejoy and this study can be found in Figure 19 (left panel). Similar trends for all molecules are observed. The
 497 exception is acetaldehyde, which was over-produced in the laboratory results of this study. The right panel of Figure 19
 498 shows a comparison of isomer abundance ratios detected in Comet 67P/CG and those from this study. The abundance
 499 ratios for Comet 67P/CG were compared by the total isomer abundances because the Rosetta Spectrometer for Ion and
 500 Neutral Analysis (ROSINA) separates by mass and could not uniquely quantify structural isomers of these organics.
 501 Therefore, the C_2H_4O isomers included, but were not limited to: acetaldehyde, ethylene oxide, and vinyl alcohol; the
 502 C_2H_6O isomers included ethanol and dimethyl ether; the $C_2H_4O_2$ isomers included methyl formate, glycolaldehyde,
 503 and acetic acid; the C_3H_6O isomers included acetone, propanal, and propylene oxide. Comet 67P/CG showed similar
 504 relative abundance ratios for the C_2H_4O and the C_2H_6O isomers as well as for the C_2H_4O and C_2H_6O isomers, which
 505 was also the case in this study. Secondly, the abundance ratios of the larger $C_2H_4O_2$ and C_3H_6O isomers were similar
 506 in Comet 67P/CG as well as in this study.

507 These two comets span a range of cometary organics with 67P/CG having more processed ices, while Lovejoy is a
 508 new dynamic Oort cloud comet with few perihelion passages. The more processed object, 67P/CG, appears to reflect
 509 abundances comparable to older interstellar objects such as Sagittarius B2(N), while Lovejoy is more comparable to
 510 the low-mass object IRAS 16293-2422(B). Both objects are in fairly good agreement within the experimental findings.
 511 This may be representative of the pristine nature of cometary volatiles being derived from simple ices recondensed in
 512 the protosolar disk, or perhaps preserved from the protosolar nebula. While these results are speculative, it suggests
 513 additional experimental studies with variation of radiation and ice composition are needed as well as more observational
 514 studies of Jupiter Family Comets (JFCs) and Oort Cloud comets.

515 Of all of the trends observed here, the most striking is the over-production of glycolaldehyde as compared to the
 516 observational studies of older star-forming regions. Astrochemical models similarly over-produce glycolaldehyde in
 517 these regions (see Garrod et al. (2008) for a detailed discussion). It is the low-mass hot core, IRAS 16298-2422(B),
 518 that most closely matches the laboratory results for all molecules, and in the case of glycolaldehyde the similarity as
 519 compared to older star-forming regions is evident. This offers intriguing insight into the possible chemical implications
 520 for these findings. As mentioned above, perhaps the laboratory study presented here better simulates the low-mass hot
 521 core scenario, which has shorter timescales for ice irradiation, warm-up, and subsequent gas-phase processing. This

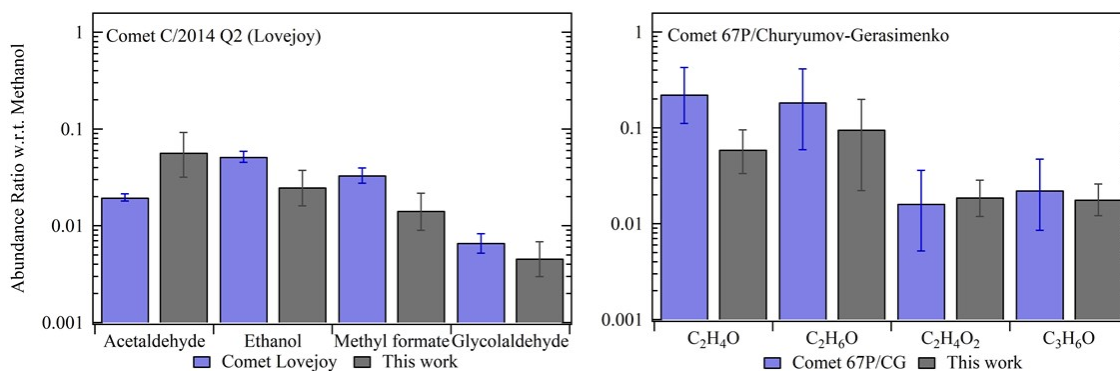


Figure 19. Abundance ratios of COMs relative to methanol as remotely detected towards Comet C/2014 Q2 (Lovejoy) (left, [Biver & Bockelée-Morvan \(2019\)](#)) and through the ROSINA mass spectrometer on the Rosetta mission in Comet 67P/Churyumov-Gerasimenko (right, [Rubin et al. \(2019b\)](#)) compared to the laboratory results from this study.

522 indicates that in high-mass hot cores there is an additional gas-phase destruction mechanism for glycolaldehyde that is
 523 not currently included in the models, nor simulated in these experiments. Again, additional experiments that explore
 524 UV fluence and warm-up timescales are warranted. Likewise, studies into potential gas-phase destruction pathways
 525 for glycolaldehyde are necessary.

526 5. CONCLUSIONS

527 Methanol ice is a potential source for complex organic molecules in interstellar clouds and possibly in comets. Here
 528 we present the UV photolysis and subsequent warm-up of a methanol ice with analysis via FTIR spectroscopy, mass
 529 spectrometry, and submillimeter/far-IR rotational spectroscopy. Nine products, all organic molecules containing more
 530 than one carbon atom, were detected in this work. In order of decreasing abundance, those photoproducts included
 531 dimethyl ether, acetaldehyde, ethanol, acetone, methyl formate, glycolaldehyde, ethylene oxide, vinyl alcohol, and
 532 ketene. The relative abundances provide evidence that the $H + CH_3O$ photodissociation pathway is favored over the
 533 $H + CH_2OH$ pathway under these experimental conditions. A technique for determining gas densities and rotational
 534 temperatures of each photoproduct was presented via a rotation diagram analysis procedure adapted for the laboratory
 535 spectroscopic technique of using lock-in detection with millimeter/submillimeter/far-IR spectroscopy. This technique
 536 provides an in-depth analysis of species that desorb from laboratory ices which allows for the determination of the
 537 rotational temperature and relative gas densities. Future studies may lead to a connection between temperature and
 538 the formation mechanisms of complex organics. Lastly, the results of this laboratory work were compared to the
 539 abundance ratios of several complex organics detected in high-mass protostar Orion-KL, low-mass protostar IRAS
 540 16293-2422(B), protocluster Sagittarius B2(N), and in comets Lovejoy and 67P/CG. Similar abundance ratios with
 541 respect to methanol were detected for many of the organics of the hot cores (specifically ethylene oxide, ethanol, methyl
 542 formate, and dimethyl ether) while the abundance ratios best matched with the low-mass protostar observations of
 543 IRAS 16293-2422(B) and comet Lovejoy.

ACKNOWLEDGMENTS

This work was supported through NASA’s Astrophysics Research and Analysis Program (NNH17ZDA001N, 17-APRA17-0030). Additional support was provided by the Planetary Science Division Internal Scientist Funding Program through the Fundamental Laboratory Research (FLaRe) work package. All experiments were conducted in the Department of Chemistry at Emory University. The authors extend special thanks to Ethan Todd and Chris Schwaiger for their assistance in characterizing the UV lamp.

544 APPENDIX

A. SUBMILLIMETER SPECTRAL ASSIGNMENT

The broadband submillimeter spectrum collected from 806500 to 812890 MHz was assigned for 5- σ peaks and can be found in the online data in Table A1. Table A1 includes the center frequency, molecule, chemical formula, and rotational quantum numbers: $J'(Ka',Kc') - J(Ka,Kc)$. Peaks marked with '?' belong to unknown features. Peaks labeled 'U' refer to transitions that are unassigned in their respective spectral catalog, but were confirmed from spectra of chemical standards.

Table A1. Submillimeter Spectral Assignment from 806500 to 812890 MHz

Peak #	Frequency (MHz)	Molecule	Formula	Transition
1	806651.41	Carbon monoxide	CO	7 - 6
2	806699.95	Ketene	C ₂ H ₂ O	40(2,39) - 39(2,38)
3	806735.82	Ketene	C ₂ H ₂ O	40(5,36) - 39(5,35); 40(5,35) - 39(5,34)
4	806877.12	Dimethyl ether	CH ₃ OCH ₃	26(6,21) - 25(5,20) EE
4	806877.61	Dimethyl ether	CH ₃ OCH ₃	26(6,21) - 25(5,20) AE
4	806878.01	Dimethyl ether	CH ₃ OCH ₃	26(6,21) - 25(5,20) AA
5	806997.05	Trans-ethanol	CH ₃ CH ₂ OH	27(7,21) - 26(6,20)

NOTE—Example table.

B. ROTATION DIAGRAM ANALYSES PARAMETERS

The calculated parameters for the rotation diagram analyses are reported in the online data in Table B1. The entries are ordered by molecule name starting with methanol. Table B1 includes the molecule name, the catalog frequency in MHz, the rotational quantum numbers: $J'(Ka',Kc') - J(Ka,Kc)$, peak area, upper state energy (E_u) in K, y-values ($\ln(\gamma WC_\tau)$), and whether the transition is reported as predicted or experimentally measured in various spectral catalogs (e.g., CDMS or JPL).

Table B1. Rotation Diagram Parameters

Molecule	Frequency (MHz)	Transition	Peak Area (K·MHz)	E_u (K)	y-value	P/E
Methanol	807508.194	13(7,6) - 14(6,8)	1972.013820	471.3191798	33.96321778	P
Methanol	807865.958	11(1,11) - 10(0,10)	76342.16587	166.3768396	35.80335572	P
Methanol	810291.478	19(8,11) - 20(7,14)	2089.324759	775.6054123	33.32670335	P
Methanol	810563.957	14(9,5) - 15(8,7)	842.4299628	652.311804	33.42394847	P
Methanol	811057.169	28(2,27) - 27(1,27)	1650.767186	1236.670497	31.50657567	P
Methanol	811247.845	12(6,6) - 11(7,4)	539.8764583	772.7872594	33.03504547	P
Methanol	811338.308	23(3,21) - 23(0,23)	585.1569982	688.4398919	33.48377331	P
Methanol	811444.546	8(2,6) - 7(1,7)	22750.39239	109.4996825	35.41524752	P
Methanol	812550.291	7(2,6) - 6(1,5)	29866.44381	102.7084283	35.76983897	P

NOTE—Example table. P/E refers to Predicted or Experimental.

REFERENCES

- 557 Abou Mrad, N., Duvernay, F., Chiavassa, T., & Danger, G. 2016, *MNRAS*, 458, 1234, doi: [10.1093/mnras/stw346](https://doi.org/10.1093/mnras/stw346)
- 558
- 559 Abou Mrad, N., Duvernay, F., Theulé, P., Chiavassa, T., & Danger, G. 2014, *AnaCh*, 86, 8391, doi: [10.1021/ac501974c](https://doi.org/10.1021/ac501974c)
- 560
- 561
- 562 Abplanalp, M. J., Gozem, S., Krylov, A. I., et al. 2016, *PNAS*, 113, 7727, doi: [10.1073/pnas.1604426113](https://doi.org/10.1073/pnas.1604426113)
- 563
- 564 Belloche, A., Müller, H. S. P., Menten, K. M., Schilke, P., & Comito, C. 2013, *A&A*, 559, A47, doi: [10.1051/0004-6361/201321096](https://doi.org/10.1051/0004-6361/201321096)
- 565
- 566
- 567 Bergantini, A., Abplanalp, M. J., Pokhilko, P., et al. 2018, *ApJ*, 860, 108, doi: [10.3847/1538-4357/aac383](https://doi.org/10.3847/1538-4357/aac383)
- 568
- 569 Biver, N., & Bockelée-Morvan, D. 2019, *ESC*, 3, 1550, doi: [10.1021/acsearthspacechem.9b00130](https://doi.org/10.1021/acsearthspacechem.9b00130)
- 570
- 571 Bockelée-Morvan, D., Lis, D. C., Wink, J. E., Despois, D., & Crovisier, J. e. a. 2000, *A&A*, 353, 1101
- 572
- 573 Bonfand, M., Belloche, A., Garrod, R. T., et al. 2019, *A&A*, 628, A27, doi: [10.1051/0004-6361/201935523](https://doi.org/10.1051/0004-6361/201935523)
- 574
- 575 Chen, Y.-J., Chuang, K.-J., Caro, G. M. M., et al. 2013, *ApJ*, 781, 15, doi: [10.1088/0004-637x/781/1/15](https://doi.org/10.1088/0004-637x/781/1/15)
- 576
- 577 Crockett, N. R., Bergin, E. A., Neill, J. L., et al. 2014, *ApJ*, 787, 112, doi: [10.1088/0004-637x/787/2/112](https://doi.org/10.1088/0004-637x/787/2/112)
- 578
- 579 Cruz-Díaz, G. A., Martín-Doménech, R., Muñoz Caro, G. M., & Chen, Y.-J. 2016, *A&A*, 592, A68, doi: [10.1051/0004-6361/201526761](https://doi.org/10.1051/0004-6361/201526761)
- 580
- 581
- 582 Drozdovskaya, M. N., van Dishoeck, E. F., Rubin, M., Jørgensen, J. K., & Altwegg, K. 2019, *MNRAS*, 490, 50, doi: [10.1093/mnras/stz2430](https://doi.org/10.1093/mnras/stz2430)
- 583
- 584
- 585 Drozdovskaya, M. N., van Dishoeck, E. F., Jørgensen, J. K., et al. 2018, *MNRAS*, 476, 4949, doi: [10.1093/mnras/sty462](https://doi.org/10.1093/mnras/sty462)
- 586
- 587
- 588 Fulvio, D., Brieva, A. C., Cuyllé, S. H., et al. 2014, *ApPhL*, 105, 014105, doi: [10.1063/1.4887067](https://doi.org/10.1063/1.4887067)
- 589
- 590 Garrod, R. T., Weaver, S. L. W., & Herbst, E. 2008, *ApJ*, 682, 283, doi: [10.1086/588035](https://doi.org/10.1086/588035)
- 591
- 592 Gerakines, P., Schutte, W. A., & Ehrenfreund, P. 1996, *A&A*, 312, 289
- 593
- 594 Goldsmith, P. F., & Langer, W. D. 1999, *ApJ*, 517, 209, doi: [10.1086/307195](https://doi.org/10.1086/307195)
- 595
- 596 Henderson, B. L., & Gudipati, M. S. 2015, *ApJ*, 800, 66, doi: [10.1088/0004-637x/800/1/66](https://doi.org/10.1088/0004-637x/800/1/66)
- 597
- 598 Hudson, R., & Moore, M. 2000, *Icar*, 145, 661, doi: <https://doi.org/10.1006/icar.2000.6377>
- 599
- 600 Hudson, R. L. 2017, *AcSpA*, 187, 82, doi: <https://doi.org/10.1016/j.saa.2017.06.027>
- 601
- Hudson, R. L., & Ferrante, R. F. 2019, *MNRAS*, 492, 283, doi: [10.1093/mnras/stz3323](https://doi.org/10.1093/mnras/stz3323)
- Hudson, R. L., Gerakines, P. A., & Ferrante, R. F. 2018, *AcSpA*, 193, 33, doi: <https://doi.org/10.1016/j.saa.2017.11.055>
- Hudson, R. L., Moore, M. H., & Cook, A. M. 2005, *AdSpR*, 36, 184, doi: <https://doi.org/10.1016/j.asr.2005.01.017>
- Hudson, R. L., Yarnall, Y. Y., & Coleman, F. M. 2020, *AcSpA*, 233, 118217, doi: <https://doi.org/10.1016/j.saa.2020.118217>
- Laas, J. C., Garrod, R. T., Herbst, E., & Weaver, S. L. W. 2011, *ApJ*, 728, 71, doi: [10.1088/0004-637x/728/1/71](https://doi.org/10.1088/0004-637x/728/1/71)
- Laas, J. C., Hays, B. M., & Widicus Weaver, S. L. 2013, *JPCA*, 117, 9548, doi: [10.1021/jp3122402](https://doi.org/10.1021/jp3122402)
- Luna, R., Molpeceres, G., Ortigoso, J., et al. 2018, *A&A*, 617, A116, doi: [10.1051/0004-6361/201833463](https://doi.org/10.1051/0004-6361/201833463)
- Maity, S., Kaiser, R. I., & Jones, B. M. 2015, *Phys. Chem. Chem. Phys.*, 17, 3081, doi: [10.1039/C4CP04149F](https://doi.org/10.1039/C4CP04149F)
- Melosso, M., Dore, L., Tamassia, F., et al. 2020, *JPCA*, 124, 240, doi: [10.1021/acs.jpca.9b10803](https://doi.org/10.1021/acs.jpca.9b10803)
- Modica, P., & Palumbo, M. E. 2010, *A&A*, 519, A22, doi: [10.1051/0004-6361/201014101](https://doi.org/10.1051/0004-6361/201014101)
- Öberg, K. I., Garrod, R. T., van Dishoeck, E. F., & Linnartz, H. 2009, *A&A*, 504, 891, doi: [10.1051/0004-6361/200912559](https://doi.org/10.1051/0004-6361/200912559)
- Paardekooper, D. M., Bossa, J.-B., & Linnartz, H. 2016, *A&A*, 592, A67, doi: [10.1051/0004-6361/201527937](https://doi.org/10.1051/0004-6361/201527937)
- Paulive, A., Shingledecker, C. N., & Herbst, E. 2020, *MNRAS*, 500, 3414, doi: [10.1093/mnras/staa3458](https://doi.org/10.1093/mnras/staa3458)
- Rubin, M., Bekaert, D. V., Broadley, M. W., Drozdovskaya, M. N., & Wampfler, S. F. 2019a, *ESC*, 3, 1792, doi: [10.1021/acsearthspacechem.9b00096](https://doi.org/10.1021/acsearthspacechem.9b00096)
- Rubin, M., Altwegg, K., Balsiger, H., et al. 2019b, *MNRAS*, 489, 594, doi: [10.1093/mnras/stz2086](https://doi.org/10.1093/mnras/stz2086)
- Schneider, H., Caldwell-Overdier, A., Coppieters 't Wallant, S., et al. 2019, *MNRASLet*, 485, L19, doi: [10.1093/mnrasl/slz019](https://doi.org/10.1093/mnrasl/slz019)
- Shingledecker, C. N., & Herbst, E. 2018, *Phys. Chem. Chem. Phys.*, 20, 5359, doi: [10.1039/C7CP05901A](https://doi.org/10.1039/C7CP05901A)
- Tercero, B., Cuadrado, S., López, A., et al. 2018, *A&A*, 620, L6, doi: [10.1051/0004-6361/201834417](https://doi.org/10.1051/0004-6361/201834417)
- Theulé, P., Endres, C., Hermanns, M., Bossa, J.-B., & Potapov, A. 2020, *ESC*, 4, 86, doi: [10.1021/acsearthspacechem.9b00246](https://doi.org/10.1021/acsearthspacechem.9b00246)
- Yocum, K. M., Smith, H. H., Todd, E. W., et al. 2019, *JPCA*, 123, 8702, doi: [10.1021/acs.jpca.9b04587](https://doi.org/10.1021/acs.jpca.9b04587)